PET/MR IMAGING OF ATHEROSCLEROTIC PLAQUE AND TUMOR USING DUAL MODALITY SPIOS

A Dissertation
Presented to
The Academic Faculty

by

Nazanin Masoodzadehgan

In Partial Fulfillment
of the Requirements for the Degree
Doctor of Philosophy in the
School of Engineering

Georgia Institute of Technology
December 2014

PET/MR IMAGING OF ATHEROSCLEROTIC PLAQUE AND TUMOR USING DUAL MODALITY SPIOS

Approved by:

Dr. Gang Bao, Ph.D., Advisor
Department of Biomedical Engineering
Georgia Institute of Technology and Emory University

Dr. Mark Goodman, Ph.D.
Department of Radiology and Imaging Sciences
Emory University

Dr. Yongjian Liu, Ph.D.
Department of Radiology
Washington University School of Medicine

Dr. Hui Mao, Ph.D.
Department of Radiology and Imaging Sciences
Emory University

Dr. Farzad Rahnema, Ph.D.
Department of Mechanical Engineering
Georgia Institute of Technology

Dr. W. Robert Taylor, MD, Ph.D.
Department of Cardiology
Emory University, Georgia Institute of Technology and Atlanta VA

Date Approved: July 29th, 2014

DEDICATION

To loving memory of my father Bahram Hoshyar, my mother Nasrin and my brothers Yousef and Behnam.

&

My husband Ata

ACKNOWLEDGEMENTS

I am extremely grateful to my thesis advisor Professor Gang Bao for the opportunity to participate in this research. His patience and guidance as an advisor and mentor have been invaluable. I would like to thank the members of my thesis committee, Dr. Mark Goodman, Dr. Yongjian Liu, Dr. Hui Mao, Dr. Farzad Rahnema, and Dr. Robert Taylor for their time and instruction. To the past and present members of Bao Lab, thank you for the foundation you have built and for your help with this research. In particular, I would like to thank Dr. Sheng Tong and Dr. Sijian Hue for being available to answer my many coating questions. This work would have been much more difficult without Dr. Johaness Leisen's help in performing MRI. I also like to thank Annie Zheng for her help with cell culture and microscopy. Also I like to thank Amy Tang for her support. I am grateful to Erin Kirshtein for her support and wonderful spirit. I also thank Dr. Charlie Glaus for his help in answering my conjugation questions. I thank Sally Gerrish for her help with career search. I also thank Glenda Johnson for her advise on graduate studies.

I especially thank Dr. Wone Woo Seo for all his help and support at Wesley Woods. This dissertation would not be completed without Wone Woo's help. I also thank the members of Dr. Goodman's group, especially Dr. Voll for always being helpful. Also, I thank Mel Kemp, Larry Williams, and Eugene Malveaux for their help with biodistribution studies. Also, I thank Aaron Smith for his help with autoradiography.

I am also thankful to Dr. Jon Nye for his help with PET imaging and teaching me image analysis. I also thank Margie Jones and Dr. Jaekun Park for her help with PET imaging.

I especially thank members of Dr. Taylors group, Diana Weiss, Sarah Knight and Jane Titterington. Also, I thank Dr. Liu's research group, Hannah and Debbie. I am grateful to Liya Wang for her help with preparing the 4T1 animal model. I also thank Dr. Ravi Bellamkonda for being a great mentor and his efforts in conducting the graduate leadership program. I also thank Dr. Garmestani for always being supportive and kind. I thank my undergraduate students, Needa Virani, Arsalan Saboori, and Samantha Gray for their outstanding work.

I also thank Nassir Mokarram for his help and advice regarding chemistry and conjugation issues and for his friendship.

Finally, I would like to thank my family for all their support during the past six years. I especially like to thank my husband Ata for his love, support and understanding.

TABLE OF CONTENTS

DEDICATION ..... **III**

ACKNOWLEDGEMENTS ..... **IV**

LIST OF FIGURES ..... **VIII**

LIST OF SYMBOLS AND ABBREVIATIONS ..... **X**

SUMMARY ..... **XI**

CHAPTER 1: DUAL MODALITY PET/MR CONTRAST AGENT **1**

Nanoparticles for PET/MR Imaging 1

SPIO Synthesis 3

SPIO Characterization 5

^{64}Cu Radiolabeling, Characterization and Serum Stability 6

Discussion and Conclusion 9

References 11

CHAPTER 2: EFFECT OF SIZE ON NANOPARTICLE PHARMACOKINETICS AND BIODISTRIBUTION **13**

Trends in vitro 14

Cellular Uptake 14

Active Targeting 18

Trends in vivo 20

Pharmacokinetics of 6nm and 14nm SPIOs 24

Biodistribution studies of 6 nm and 14 nm SPIOs 27

Discussion and Conclusion 32

References 33

Chapter 3: IN VIVO IMAGING OF EARLY STAGE ATHEROSCLEROTIC PLAQUES **38**

Atherosclerosis 38

VCAM1 Targeting 39

Plaque Imaging 42

In Vitro Targeting Studies 44

Phantom Studies 45

Carotid Ligation Model 46

In vivo and Ex vivo imaging using DiR labeled SPIOs 47

In vivo PET/CT imaging using ^{64}Cu-VINP-SPIOs 49
Discussion and Conclusion 51
References 53
CHAPTER 4: TUMOR IMAGING 55
In vivo imaging of 4T1 Tumor 56
Surface coating and functionalizing ^{64}Cu-CD105 Targeted SPIOs 60
Phantom Studies 64
Radiolabeling and characterization 65
4T1 Tumor Model 66
PET Imaging and Biodistribution studies of CD105 Targeted SPIOs 67
In vivo MR imaging using ^{64}Cu-CD105-SPIOs 70
Discussion and Conclusion 71
References 74
CHAPTER 5: CONCLUSIONS AND FUTURE CHALLENGES 77
APPENDIX A: 81
APPENDIX B: 82
CURRICULUM VITA 85

LIST OF FIGURES

Page

FIGURE 1, SCHEMATIC OF SPIO NANOPARTICLE. 3

FIGURE 2, SCHEMATIC OF THE SYNTHESIS OF ^{64}CU-VINP-SPIO. 4

FIGURE 3, CHARACTERIZAITON OF SPIOS USING TEM. 6

FIGURE 4 CHARACTERIZAITON OF ^{64}CU RADIOLABELED SPIOS USING RADIO-TLC. 7

FIGURE 5, TITRATION EXPERIMENT TO DETERMINE THE NUMBER OF BAT CHELATORS. 8

FIGURE 6, MOUSE SERUM STABILITY OF TARGETED AND NON-TARGETED ^{64}CU-SPIOS. 9

FIGURE 7, SCHEMATIC DEPICTING THE EFFECT OF NANOPARTICLE SIZE ON THE MEMBRANE WRAPPING PROCESS. 16

FIGURE 8, SCHEMATIC REPRESENTS THE RELATIONSHIP BETWEEN NANOPARTICLE SIZE AND CIRCULATION HALF-LIFE. 22

FIGURE 9, CHARACTERIZAITON OF 6 NM AND 14 NM SPIOS USING TEM, DLS DIAMETER AND ZETA POTENTIAL MEASUREMENTS. 25

FIGURE 10, BLOOD CIRCULATION HALF-LIFE OF ^{64}CU-VINP-SPIOS AND ^{64}CU-VINP-SPIOS WITH SEVERAL VARIATION OF SIZE AND PEG DENSITY. 27

FIGURE 11, BIODISTRIBUTION DATA OF 14 NM NON-TARGETED ^{64}CU-DOTA-SPIO . 28

FIGURE 12, BIODISTRIBUTION DATA OF 6NM NON-TARGETED ^{64}CU-SPIO IN BLACK C57 MICE. 29

FIGURE 13, BIODISTRIBUTION DATA OF 6NM TARGETED ^{64}CU-SPIO IN BLACK C57 MICE. 30

FIGURE 14, BIODISTRIBUTION DATA OF 14NM NON-TARGETED ^{64}CU-SPIO IN BLACK C57 MICE. 31

FIGURE 15, BIODISTRIBUTION DATA OF 14NM TARGETED ^{64}CU-SPIO IN BLACK C57 MICE. 32

FIGURE 16, THE PROGRESSION OF AN ATHEROSCLEROTIC LESION[49]. 39

FIGURE 17, IN VITRO INVESTIGATION OF VINP-SPIOS WITH IMAECS. SCALE BAR = 10 µM 45

FIGURE 18, PHANTOMPET IMAGE OF ^{64}CU-VINP-SPIOS. 46

FIGURE 19, CAROTID LIGATION MODEL AND EXPERIMENTAL SET UP..... 47

FIGURE 20, REPRESENTATIVE IN VIVO NIRF IMAGING OF CAROTID LIGATION BLACK C57 MICE..... 47

FIGURE 21, EX VIVO CAROTID ARTERY ANALYSIS SPIOS..... 48

FIGURE 22, MICROPET/MICROCT IMAGES OF INFLAMMATION 50

FIGURE 23, QUANTITATIVE IMAGE ANALYSIS OF ACCUMULATION OF SPIOS 51

FIGURE 22, SCHEMATIC OF THE SYNTHESIS OF ^{64}CU-CD105-SPIO..... 61

FIGURE 23, SIZE DISTRIBUTION OF BAT-SPIOS AND BAT-CD105-SPIOS USING DLS 62

FIGURE 24, IN VITRO INVESTIGATION OF SPIOS IN CD105 POSITIVE HUVECS..... 63

FIGURE 25, IN VITRO INVESTIGATION OF SPIOS IN CD105 NEGATIVE CELLS..... 64

FIGURE 26, CHARACTERIZATION OF CD105 SPIOS. PHANTOM MR IMAGE OF NANOPARTICLES 65

FIGURE 27, RADIOTLC ANALYSIS OF CRUDE SAMPLE OF ^{64}CU-CD105-SPIO..... 65

FIGURE 28, FEMALE BALB/C MICE WITH TWO 4T1 TUMORS SHOWN WITH RED ARROWS..... 66

FIGURE 29, REPRESENTATIVE MICROPET/MICROCT IMAGES OF 4T1 TUMOR. 67

FIGURE 30, BIODISTRIBUTION OF ^{64}CU-CD105-SPIOS AND NON-TARGETED ^{64}CU-SPIOS..... 68

FIGURE 31, REPRESENTATIVE MICROPET/MICROCT IMAGES OF 4T1 TUMOR..... 69

FIGURE 32, REPRESENTATIVE MR IMAGES OF 4T1 TUMOR 24 HR..... 71

LIST OF SYMBOLS AND ABBREVIATIONS

CT	Computed Tomography
CRP	C-reactive protein
DI	Deionized
3D	Three-Dimensional
DLS	Dynamic Light Scattering
DI	Deionized
DMEM	Dulbecco's Modified Eagle Medium
hr	hour(s)
DMSO	Dimethyl Sulfoxide
DOTA	1,4,7,10-tetraazacyclododecane-1,4,7,10-tetraacetic acid
DSPE	1,2-Distearoyl-sn-Glycero-3-Phosphoethanolamine
DTPA	Diethylene triamine pentaacetic acid
EDTA	Ethlenediaminetetraacetic Acid
FPLC	Fast Protein Liquid Chromatography
HCl	Hydrochloric acid
HPLC	High Performance Liquid Chromatography
IACUC	Institutional Animal Care and Use Committee
IR	Infrared
MEA	Mercaptoethylamine
LPS	Lipopolysaccharide
nm	nanometer(s)
MRI	Magnetic Resonance Imaging
MW	Molecular Weight
RT	Room Temperature
NIRF	Near Infrared Fluorescence
OCT	Optical Coherence Tomography
PBS	Phosphate Buffered Saline
PEG	Polyethylene Glycol
PET	Positron Emission Tomography
SEM	Scanning Electron Microscopy
SPIO	Superparamagnetic Iron Oxide
T1	Longtitudinal relaxation time T1
T2	Transverse relaxation time T2
TEM	Transmission Electron Microscopy
TLC	Thin Layer Chromatography
VCAM	Vascular Cell Adhesion Molecule
VINP	VHPKQHRGGSYGC

SUMMARY

Diagnosis and treatment of disease in its early stages is often the key to success. The 20th century saw impressive applications of engineering technology in early stage diagnosis, as well as the application of such technology in other fields of medicine. Taking advantage of the new development in the field of material science and synthetic techniques for developing nanoparticles, the field of nanomedicine has emerged and one of its goals is to diagnose early stage disease when it is still at molecular level. By allowing for the non-invasive and quantitative detection of disease biomarkers, nanoparticles provides substantial improvements in both specificity and sensitivity of diagnostic imaging [1-4].

The unique properties of nanoparticles provide a new platform in molecular imaging for early detection of diseases such as cancer and atherosclerosis. One class of nanoparticles are superparamagnetic iron oxide nanoparticles (SPIOs), which consist of an iron oxide core with a PEG coating that can be functionalized with a targeting ligand and a radiotracer. The targeting agent can be selected to recognize a disease biomarker therefore, enhancing the contrast between malignant and benign tissue. The radiotracer will enable imaging with PET (positron emission tomography) which has the highest sensitivity among all imaging modalities [5]. The large surface area of the SPIO enabled labeling with high specific activity leading to significant increase in sensitivity of the detection. SPIOs can be loaded with reporter molecules such as radionuclide and targeting proteins and peptides. In our lab, we have developed a new method for synthesizing SPIOs with tight control over their diameter and surface chemistry [6].

Due to the continuous exposure of atherogenic factors, molecular events occurring at the endothelium contribute significantly to the development of atherosclerotic plaques. In particular, endothelial expression of adhesion molecules such as vascular cell adhesion molecule (VCAM1), which is involved in leukocyte recruitment, plays a critical role in the earliest stages of atherogenesis. Detection of molecular markers of early-stage atherosclerotic plaques such as VCAM-1 requires high sensitivity targeting. Although methods based on various medical imaging modalities, including ultrasound, X-ray computed tomography (CT) and MRI, have been developed and utilized for detecting plaque volume and constituents and for visualizing the vessel lumen and the vessel wall, PET imaging is the most sensitive human molecular imaging modality for plaque detection, since it can produce whole body images for functional and molecular information. Therefore, emphasis in our in vivo imaging studies will be placed on developing nanoparticle-based contrast agents for PET imaging [7, 8]. Further, there are multitudes of PET tracers available to use for conjugation to many types of nano agents. With applications ranging from clinical and research in neurology and cardiology PET/MR allows for imaging in the main processes of cancer development: apoptosis resistance, angiogenesis, proliferation and metastasis [9].

This thesis established the ability to develop a functionalized PEG coating for the SPIOs which allows for labeling with both ^{64}Cu and targeting ligand to recognize the disease biomarker. This will provide a platform for pre-clinical in vivo imaging of disease using multi modal SPIO nanoparticles.

CHAPTER 1

DUAL-MODALITY PET/MR CONTRAST AGENT

Nanoparticles for PET/MR Imaging

Nanoparticles used as a molecular imaging tool with extensive multifunctionality and flexibility provide platforms for targeting the specific disease biomarkers and integration of imaging modalities. One such molecular imaging tool is super paramagnetic iron oxide nanoparticles, SPIOs, widely used as Magnetic Resonance (MR) contrast agent. SPIOs can be labeled with ^{64}Cu to investigate their potential for multi modal positron emission tomography (PET) MR imaging. Dual modality PET MR SPIO contrast agent can be synthesized to image diseases such as cancer and atherosclerosis. Positron emission tomography (PET) imaging is now the standard clinical diagnostic modality for staging and restaging of cancer and is one of the few molecular imaging techniques approved by the FDA. The advantage is the non-invasive and early detection of disease at molecular lever before it has spread to late stages or in case of the atherosclerosis before the plaque has blocked the vessel [10, 11].

Positron Emission Tomography (PET) was created in 1970s to combine early biochemical assessment of pathology with the precise localization through the use of nuclear medicine and computerized image reconstruction. In this technique a biologically active chemical compound is labeled with a radioactive isotope that decays by emitting a positron. The positron then travels a small distance before combining with an electron and emitting two gamma photons [19]. This technology has a very high sensitivity compared to other image modalities and PET images can be interpreted to provide regional assessment of biochemical processes. The lack of anatomical information was

solved by combining PET with high resolution anatomical imaging like Computed Tomography (CT) in the late 1990s [20]. However, increased use of the CT which is associated with ionizing radiation has led to concern among the radiology community (radiologists, medical physicists, and manufacturers) [21]. Combination of PET and MR is an attractive option since MR provides high anatomical resolution without the harmful effects of ionizing radiation and much effort has been invested in developing a PET/MR diagnostic imaging system [22, 23]. To better visualize the existence of malignancy with this system, a dual modality contrast agent such as radio-labeled SPIO is developed. Dual modality PET MR SPIO contrast agent can be synthesized to image diseases such as cancer and atherosclerosis. The advantage is the non-invasive and early detection of disease at molecular lever before it has spread to late stages or in case of the atherosclerosis before the plaque has blocked the vessel. There are however many challenges in the development of the multi-modal PET MR contrast agent. The radionuclide used for PET imaging has a limited half-life; also chemical conjugation methodologies must be developed to ensure that the particle stays intact after it is exposed to the harsh environment inside the body [24].

The unique decay properties of ^{64}Cu make it useful as a radiotracer for PET. It has a longer half life (12.701 ± 0.002 hours) compared to FDA approved ^{18}F and decays by 17.86% positron emission, 39.0% by beta decay, 43.075% by electron capture and 0.475% gamma radiation/internal conversion. The half-life of 12.7 hours makes ^{64}Cu appropriate for radiosynthesis and allows for imaging 24 hrs post injection. The beta-decay makes it appropriate for radiotherapy as well. Another main advantage is the low radiation burden and the wide application in clinical investigations. It can also be

produced in high yield and high specific activity which is required for in-vivo PET imaging [25].

Figure 1 shows the schematic of the SPIO nanoparticle with the Fe_3O_4 core, and functionalized PEG coating that allows for conjugation of targeting ligands, NIRF dyes, and metal chelators.

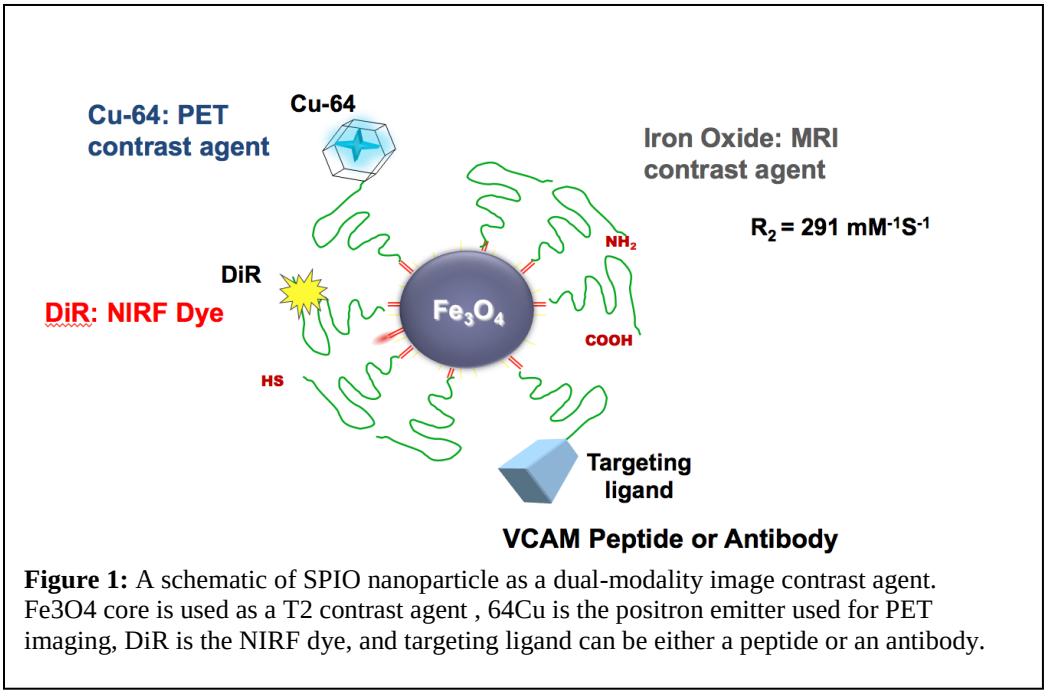

Figure 1: A schematic of SPIO nanoparticle as a dual-modality image contrast agent. Fe3O4 core is used as a T2 contrast agent , 64Cu is the positron emitter used for PET imaging, DiR is the NIRF dye, and targeting ligand can be either a peptide or an antibody.

SPIO Synthesis

Figure 2 shows the schematic of the synthesis of ^{64}Cu-VINP-SPIO. Iron cores were coated with DSPE-PEG2k-methoxy, DSPE-PEG-maleimide, and lipid-PEG-BAT to prepare them for dual PET/MR imaging. Macrocyclic ligand BAT allows for radiolabeling by chelating of copper 64. The maleimide coating of the nanoparticles provide a site for attachment of VINP peptide.

Figure 2 shows the major steps toward the synthesis of ^{64}Cu-VINP-SPIOs. Uniform Fe_3O_4 iron cores (1) were first pegylated with lipid-PEG-BAT, DSPE-PEG-

methoxy, and DSPE-PEG-maleimide (2), which was subjected to VINP peptide conjugation (3). ^{64}Cu labeling was performed in the last step to generate ^{64}Cu-BAT-VINP-SPIO (4).

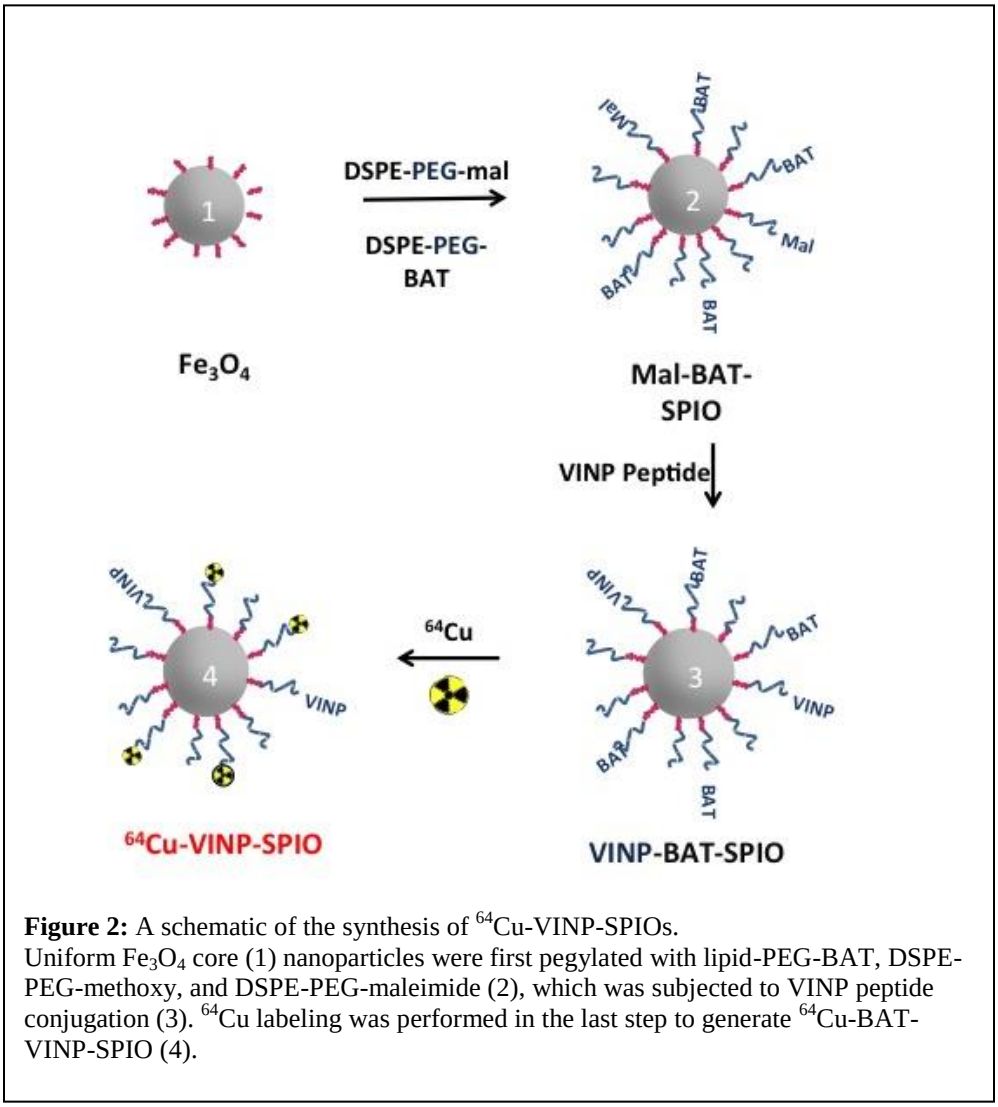

Figure 2: A schematic of the synthesis of ^{64}Cu-VINP-SPIOs.
Uniform Fe_3O_4 core (1) nanoparticles were first pegylated with lipid-PEG-BAT, DSPE-PEG-methoxy, and DSPE-PEG-maleimide (2), which was subjected to VINP peptide conjugation (3). ^{64}Cu labeling was performed in the last step to generate ^{64}Cu-BAT-VINP-SPIO (4).

This simplified synthesis scheme has a great advantage over previously reported schemes. With this method, there is no need for post conjugation of the chelator for ^{64}Cu. This leads to higher nanoparticle stability and radioactive yield. There is also a much

improved control over the amount of chelators that can be incorporated into the SPIO nanoparticles. This allows us to modulate the radioactive yield depending on the application.

SPIO Characterization

The number of VCAM targeting VINP peptides per nanoparticle was measured by using an Abcam maleimide quantification assay on maleimide activated nanoparticles before and after peptide conjugation. The difference in thiol concentration between Mal-BAT-SPIO and VINP-BAT-SPIO was used to calculate the average number of VINP peptides conjugated to Mal-BAT-SPIO.

The hydrodynamic diameter and surface potential of Mal-BAT-SPIO and VINP-BAT-SPIO was measured by dynamic light scattering (DLS). DLS measurements were performed using a Malvern Zetasizer Nano ZS. Samples were measured in triplicate (with 5 runs each) at 25 °C and data are reported as the average ξ potential (mV).
Iron concentration of Mal-BAT-SPIO and VINP-BAT-SPIO solutions was determined using a Ferrozine assay.

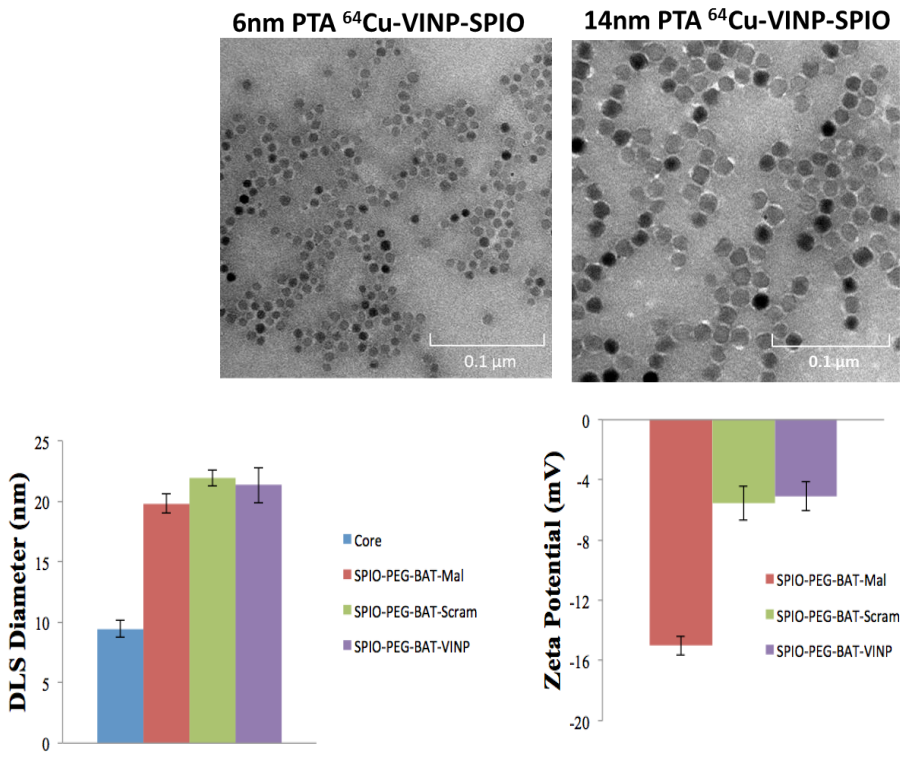

Figure 3: Characterization of SPIOs using TEM, DLS diameter and zeta potential measurements. A TEM image of 6nm ^{64}Cu-BAT-VINP-SPIO and 14nm ^{64}Cu-BAT-VINP-SPIO is shown on the top. DLS size (left) and zeta potential (right) changes of SPIO after conjugation with VINP and scramble peptide.

^{64}Cu Radiolabeling, Characterization and Serum Stability

Radiolabeling of BAT-VINP-SPIOs was obtained by incubation with ^{64}Cu at 37 °C for 1 hr in 0.1 M ammonium acetate buffer, pH 5.5. In this study ^{64}Cu-VINP-SPIOs was labeled to a specific activity of 45 µCi/µg. Nonspecifically bound ^{64}Cu was removed by addition of EDTA upon completion of the labeling reaction, and ^{64}Cu-EDTA was separated from ^{64}Cu-VINP-SPIOs using filter centrifugation. Quality control was performed to characterize the percent yield and radio chemical purity.

A small amount of the of the ^{64}Cu SPIO solution was applied to an ITLC-SG plate (Pall Corporation, East Hills, NY) and developed using a 1:1 mixture (v/v) of 10% (w/v) ammonium acetate and methanol (Rf = 0 for ^{64}Cu–SPIO and Rf = 1 for ^{64}Cu-EDTA and ^{64}Cu-acetate). The TLC plate was then measured using a Rita Star (Raytest, Straubenhardt, Germany).

Radiochemical purity (RCP) of ^{64}Cu SPIO was evaluated by radio-fast protein liquid chromatography (radio-FPLC) using an Amersham Biosciences ÄKTA FLPC system (GE Healthcare, Piscataway, NJ) equipped with a UV detector (280nm) and fitted with an in-line Flow-Count radioisotope detector (Bioscan, Poway, California). A 100 µL sample of dilute ^{64}Cu-SPIO was applied to a Superose 12 gel filtration column (GE Healthcare, Piscataway, NJ) and eluted with 20 mM HEPES and 150 mM NaCl (pH 7.3) at a flow rate of 0.8 mL/min. The RCP of ^{64}Cu –SPIO was found to be > 98%. The nanoparticle solution was then diluted in PBS (pH 7.4) to obtain doses (10-100 µCi) suitable for biodistribution and PET imaging studies.

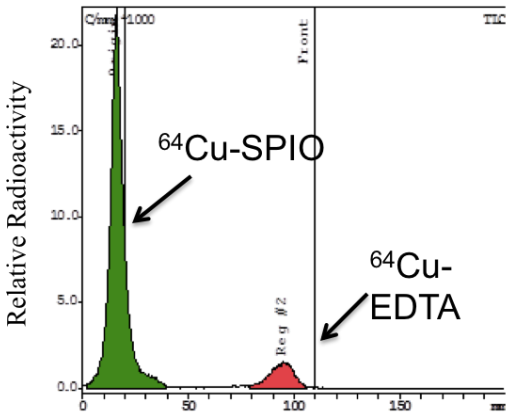

Figure 4: Characterization of ^{64}Cu radiolabeled SPIOs using radio-TLC.
^{64}Cu-SPIOs (90%) are shown in the green peak and the free ^{64}Cu-EDTA is shown as the red peak (10%).

The number of BAT groups available to chelate the Cu was estimated by adding 100 µg of the nanoparticles to a known excess of "hot plus cold" Cu-acetate. After 1 hr incubation at 37 ^{o}C, a 10mM EDTA was added and the resulting solution was incubated for 5 min at 37 ^{o}C. Aliquotes were then analyzed by radio-TLC. The percent labeling yield increased as the amount of cold copper decreased as shown in Figure 4. The number of BAT chelators attached to the SPIO was determined from the following equation:

$$n(chelates) = \frac{n(copper) \times LabelingEfficiency(\%)}{100}$$

According to the above equation, the number of BAT chelates was determined to be 4.

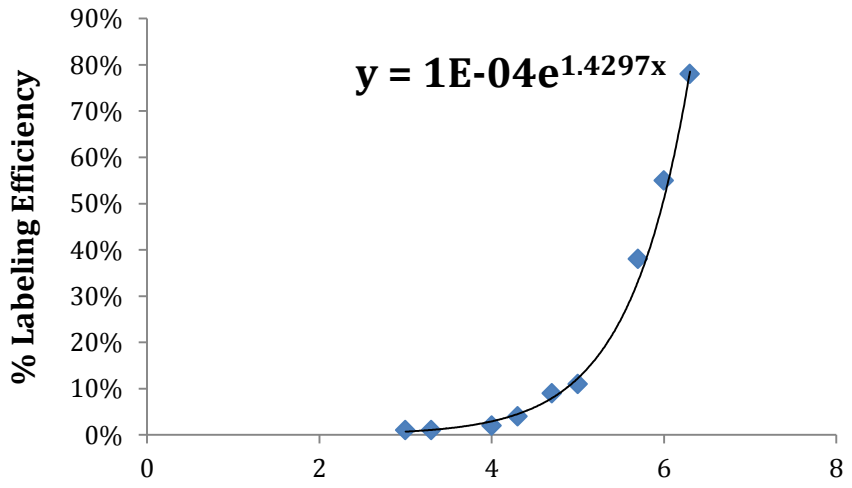

Figure 5: Titration experiment to determine the number of BAT chelators per particle.

Serum stability of ^{64}Cu–SPIO was measured by radio-TLC and radio-FPLC analysis after 0, 1, 3, and 24 hr incubation in mouse serum at 37°C with constant shaking. A 100 ul volume of SPIO solutions with 100 ul of mouse serum at 37^{o}C up to 24 hr. A small aliquots was injected to the radioFPLC and % bound activity was calculated for each time point.

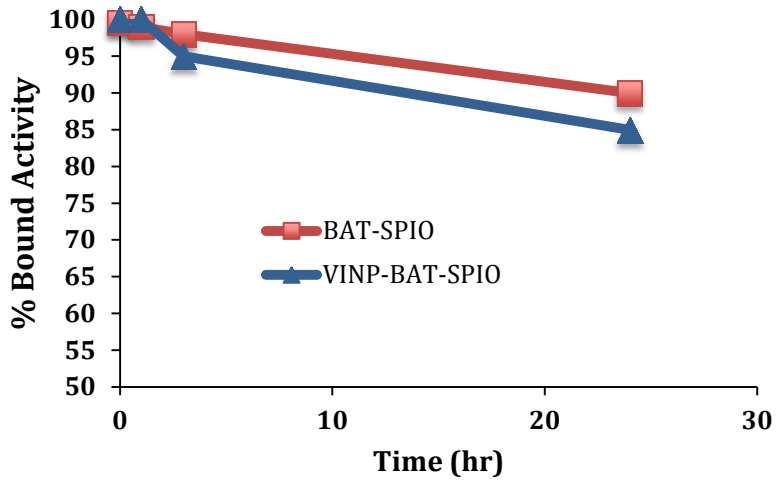

Figure 6: Mouse serum stability of Targeted and non-targeted ^{64}Cu-SPIOs analyzed using radio FPLC.

As shown in Figure 6, serum stability showed that both VCAM targeted ^{64}Cu-SPIOs and non- targeted ^{64}Cu-SPIOs are stable in mouse serum up to 24 hr and less than 10% dissociation of ^{64}Cu or degradation of SPIOs was observed.

Discussion and Conclusion

We developed a simplified method for developing radiolabeled targeted SPIOs. This method takes advantage of the chelator BAT that is conjugated to the PEG before the coating process begins. This conjugation eliminated a need for post conjugation of the chelator DOTA and significantly improved the radiolabeling yield. It also allowed for the incorporation of DSPE-PEG2k-maleimide and conjugation of the targeting peptide. Chelator BAT which is a derivative of TETA has higher affinity for ^{64}Cu compared to DOTA. This leads to higher *in vivo* stability and overall particle stability as is shown in the serum stability results. We characterized the particle size, radiochemical yield and serum stability to make sure it is suitable for *in vivo* imaging applications. Although the radiolabeling yield was very high (90%) with only 10% free ^{64}Cu-EDTA, we performed

four rounds of filter centrifugation to wash and purify the SPIOs from free ^{64}Cu and reaction buffer. The final sample had a radiochemical purity of higher than 99% and was dissolved in PBS for further *in vitro* and *in vivo* studies. SPIOs had a very uniform size distribution after coating and conjugation as shown in TEM and DLS results. The particles uniform size distribution and functionalized PEG coating allows for improved characteristics over the existing iron oxide nanoparticles. A titration experiment was performed with a mixture of hot and cold copper to estimate the number of BAT chelators. On average there were 15 chelators per particle. A specific peptide sequence which is shown to be specific for VCAM1, VINP (VHPKQHRGGSYGC) was conjugated to the maleimide group to make ^{64}Cu-VINP-SPIOs. We explored the use of anti-VCAM antibody but found the use of VINP peptide beneficial in comparison. To confirm specificity, we also tested a modified version of the SPIO conjugated to scramble peptide (PRHKVQHGGSYGC). The peptide is smaller than the antibody which leads to longer circulation half-life. The conjugation of the peptide is easier when compared to antibody and it is cost efficient. This peptide targeted particle was used in the biodistribution and PET imaging studies of inflammation. Although there are challenges in the efficient synthesis of SPIOs, they have a great potential in being used in pre-clinical imaging.

The dual modality of SPIOs allows for imaging with both PET and MRI. PET imaging provides high sensitivity while MRI has very high soft tissue contrast. Although PET and MRI systems are not combined and we will perform our studies on separate systems, we hope that in the future this nanoparticle be translated to clinic for use as a contrast agent on a combined PET/MR imaging system.

References

1. Thorek, D.L., et al., *Superparamagnetic iron oxide nanoparticle probes for molecular imaging.* Ann Biomed Eng, 2006. **34**(1): p. 23-38.

2. Cheng, Z., D.L. Thorek, and A. Tsourkas, *Gadolinium-conjugated dendrimer nanoclusters as a tumor-targeted T1 magnetic resonance imaging contrast agent.* Angew Chem Int Ed Engl, 2010. **49**(2): p. 346-50.

3. Tsourkas, A., et al., *In Vivo Imaging of Activated Endothelium Using an Anti-VCAM-1 Magnetooptical Probe.* Bioconjugate Chemistry, 2005. **16**(3): p. 576-581.

4. Zhang, C.Y., J. Lu, and A. Tsourkas, *Iron chelator-based amplification strategy for improved targeting of transferrin receptor with SPIO.* Cancer Biol Ther, 2008. **7**(6): p. 889-95.

5. Jarrett, B.R., et al., *In Vivo Mapping of Vascular Inflammation Using Multimodal Imaging.* PLoS ONE, 2010. **5**(10): p. e13254.

6. Tong, S., et al., *Coating Optimization of Superparamagnetic Iron Oxide Nanoparticles for High T2 Relaxivity.* Nano Letters, 2010. **10**(11): p. 4607-4613.

7. Nahrendorf, M., et al., *Nanoparticle PET-CT imaging of macrophages in inflammatory atherosclerosis.* Circulation, 2008. **117**(3): p. 379-87.

8. Nahrendorf, M., et al., *Noninvasive vascular cell adhesion molecule-1 imaging identifies inflammatory activation of cells in atherosclerosis.* Circulation, 2006. **114**(14): p. 1504-11.

9. Wehrl, H.F., et al., *Combined PET/MR imaging--technology and applications.* Technol Cancer Res Treat, 2010. **9**(1): p. 5-20.

10. Caravan, P., et al., *Gadolinium(III) Chelates as MRI Contrast Agents: Structure, Dynamics, and Applications.* Chemical Reviews, 1999. **99**(9): p. 2293-2352.

11. Sun, C., J.S. Lee, and M. Zhang, *Magnetic nanoparticles in MR imaging and drug delivery.* Adv Drug Deliv Rev, 2008. **60**(11): p. 1252-65.

12. Rossin, R., et al., *In Vivo Imaging of 64Cu-Labeled Polymer Nanoparticles Targeted to the Lung Endothelium.* Journal of Nuclear Medicine, 2008. **49**(1): p. 103-111.

13. Kelly, K.A., et al., *Detection of vascular adhesion molecule-1 expression using a novel multimodal nanoparticle.* Circulation Research, 2005. **96**(3): p. 327-336.

14. Nahrendorf, M., J.R. McCarthy, and P. Libby, *Over a Hump for Imaging Atherosclerosis Nanobodies Visualize Vascular Cell Adhesion Molecule-1 in Inflamed Plaque.* Circulation Research, 2012. **110**(7): p. 902-903.

15. Kaufmann, B.A., et al., *Molecular imaging of inflammation in atherosclerosis with targeted ultrasound detection of vascular cell adhesion molecule-1.* Circulation, 2007. **116**(3): p. 276-284.

16. Toth, P.P., *Atherosclerosis: The Underlying Disease.* The Journal of Family Practice, 2009. **58**(11).

17. Boudi, F.B., et al. *Coronary Artery Atherosclerosis*. Medscape Reference-Drugs, Diseases & Procedures, 2009.

18. Crowther, M., *Pathogenesis of Atherosclerosis.* American Society of Hematology, 2005.

19. Insull, W., *The Pathology of Atherosclerosis: Plaque Development and Plaque Responses to Medical Treatment.* American Journal of Medicine, 2009. **122**(1): p. S3-S14.

20. Osborn, E.A. and F.A. Jaffer, *The Year in Molecular Imaging.* JACC: Cardiovascular Imaging, 2010. **3**(11): p. 1181-1195.

21. Nahrendorf, M., et al., *Noninvasive vascular cell adhesion molecule-1 imaging identifies inflammatory activation of cells in atherosclerosis.* Circulation, 2006. **114**(14): p. 1504-1511.

22. Iiyama, K., et al., *Patterns of vascular cell adhesion molecule-1 and intercellular adhesion molecule-1 expression in rabbit and mouse atherosclerotic lesions and at sites predisposed to lesion formation.* Circulation Research, 1999. **85**(2): p. 199-207.

23. Ferrante, E.A., et al., *Dual targeting improves microbubble contrast agent adhesion to VCAM-1 and P-selectin under flow.* Journal of Controlled Release, 2009. **140**(2): p. 100-107.

24. Jaffer, F.A., P. Libby, and R. Weissleder, *Molecular and cellular imaging of atherosclerosis - Emerging applications.* Journal of the American College of Cardiology, 2006. **47**(7): p. 1328-1338.

25. Thorek, D.L.J., et al., *Superparamagnetic Iron Oxide Nanoparticle Probes for Molecular Imaging.* Annals of Biomedical Engineering, 2006. **34**(1): p. 23-38.

CHAPTER 2

EFFECT OF SIZE ON NANOPARTICLE PHARMACOKINETICS AND BIODISTRIBUTION

In the past 30 years, nanotechnology has become a promising strategy for diagnostic, imaging, and therapeutic applications [1]. Altering a nanoparticle's size, shape, and surface chemistry allows nanoparticles to be tailored to different functions [2, 3, 4]. Nanoparticles are rendered useless, however, if they do not first reach the targeted tissue. Rapid clearance of nanoparticles from the human body by the mononuclear phagocyte system (MPS) and reticuloendothelial system (RES) is one of the biggest obstacles to ensuring that nanoparticles reach their target [1, 5]. Alterations of nanoparticle size attempt to modulate the pharmacokinetics and temporarily prevent clearance from the blood [5, 6]. Successful evasion of the RES for certain time points post-injection can be observed by measuring blood circulation half-life and examining the biodistribution of nanoparticles in the blood, the RES organs, and the targeted tissue [6]. Currently, nano-bio interactions are being studied so that design specifications may be established to aid in the development of nanodevices with properties that allow them to reach the targeted tissue [1].

When designing nanoparticles, the specific functionality must be considered. For example, nanoscale therapeutics for tumors relies on cellular uptake and tumor permeability. Both of these factors depend on a nanoparticle's size [1, 7, 8]. Likewise, nanoparticles used to enhance an imaging modality have size-dependent properties. The size of the nanoparticle will affect uptake by targeted cells, as well as both positive and

negative contrast in an image [9, 10, 11]. The specific location and type of targeted tissue will also impact the ideal size of a nanoparticle [12].

Developing a complete understanding of the effects that nanoparticle size has on various functionalities is crucial. As these effects are discovered, general rules can emerge that can be applied to models, making them more accurate [13]. Models can streamline future nanoparticle construction and provided a quantitative relationship between nanoparticle size and biodistribution [13]. The current state of knowledge regarding the *in vitro* and *in vivo* effects of nanoparticle size, specifically in therapeutic and diagnostic applications, is summarized in this review.

Trends *in vitro*

There is a growing interest in investigating the *in vitro* effects of nanoparticle size [13]. Numerous *in vitro* studies have been conducted, which involve different cell types, probes with various core materials, surface charges, and tested size ranges [4, 5, 9, 15, 16, 30]. These studies show size-dependent trends in cellular uptake and active targeting. In this review, an analysis of the specific *in vitro* trends will be discussed, with some high impact studies highlighted in Table 1.

Cellular Uptake

Nanoparticle shape, core composition, and size are strong determinants of cellular uptake [1]. Nanoparticle shape, whether spherical, cubic, rod-like, or worm-like, influences cellular uptake [18, 17]. In a comparison between cubic, spherical, and rod-like gold nanoparticles, spherical particles showed the highest uptake in terms of weight, on the other hand rod-like nanoparticles showed the highest uptake in terms of quantity

[18]. DOX-loaded polymeric nanoparticles showed a similar trend, with a higher cellular uptake in MCF-7 cells observed for rod-like and worm-like nanoparticles than spherical nanoparticles [17].

Nanoparticle size also impacts cellular uptake due to its influence on the enthalpic and entropic properties that govern the adhesion strength between nanoparticles and cellular receptors [3]. Zhang *et al.* developed a thermodynamic model that showed optimal cellular uptake when a ligand-coated nanoparticle is 50 nm in diameter [14]. In experimental studies with HeLa cells, a spherical nanoparticle with a 50 nm diameter showed the highest cellular uptake [15]. In addition, a targeting study using gold nanoparticles reported the highest cellular uptake with 40-50 nm diameter gold nanoparticles in SKBR-3 cells [16]. The same trend was observed when the core was changed from gold to silver [16].

As shown in an illustration in Figure 7, size-dependent uptake is likely related to the membrane-wrapping process that a nanoparticle undergoes during endocytosis [1, 14]. Due to a ligand shortage, small nanoparticles must bind to receptors in close proximity to drive the membrane-wrapping process. The enthalpic limit occurs at a nanoparticle size of about 30 nm, meaning particles smaller than this limit will not drive the membrane-wrapping process effectively [19]. Small nanoparticles also tend to dissociate from the cellular receptors before endocytosis can occur [16]. In contrast, large nanoparticles drive the membrane-wrapping process by binding to many receptors; however, a nanoparticle above 60 nm results in a receptor shortage, which decreases uptake because of the increasing entropic penalty [19]. Although the exact optimal diameter varies between applications, a nanoparticle between 30 and 60 nm in diameter

can recruit and bind to enough cellular receptors to drive the membrane-wrapping process without a receptor shortage affecting endocytosis [14, 19]. Most *in vitro* studies show a maximum cellular uptake within the 30-60 nm range, regardless of core composition or surface charge [5, 9, 15, 20].

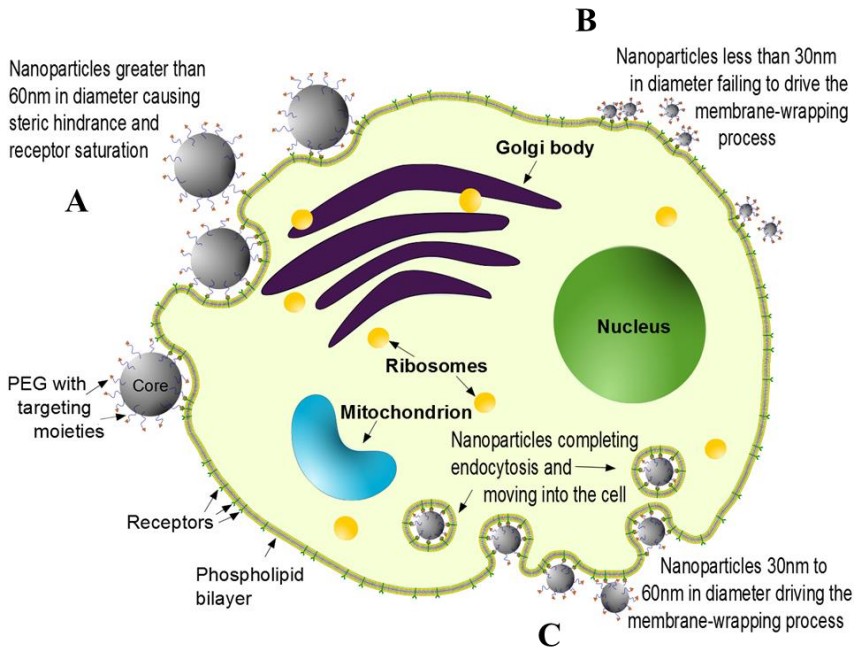

Figure 7: A schematic depicting the effect of nanoparticle size on the membrane wrapping process. Nanoparticles greater than 60 nm in diameter driving the membrane-wrapping process by binding to a large number of receptors but limiting the binding of other nanoparticles (A). Nanoparticles less than 30 nm in diameter attaching to some membrane receptors but failing to drive the membrane-wrapping process unless many bind to receptors in close proximity (B). Nanoparticles between 30 nm and 60 nm in diameter attaching to membrane receptors and driving the membrane-wrapping process effectively (C).

Other parameters affecting cellular uptake are surface charge and cell type. Liu *et al.* conducted a study comparing the uptake of a range of gold nanoparticle sizes with both positive and negative surface charges. In phagocytic cells, positively-charged nanoparticles showed higher uptake for each size [5]. Interestingly, the positively-charged nanoparticles showed the greatest uptake with a 58 nm diameter particle, but the negatively-charged particles showed the greatest uptake with a 40 nm diameter particle

[5]. Likewise, nonphagocytic cells showed a significant increase in the uptake of positively-charged particles compared to negatively-charged particles. Again, the maximum uptake of negatively-charged particles was seen with a 40 nm diameter, while the maximum uptake of positively-charged nanoparticles was seen in particles with a 58 nm diameter [5]. Further comparison shows no definite size-dependent trend in the uptake of positively-charged particles, but negatively-charged particles showed a trend of higher uptake at 40 nm [5]. Drug-loaded polymeric nanoparticles were tested in a similar manner, and showed similar results regarding the effects of surface charge. The macrophage cells showed increased uptake with increased nanoparticle size, while non-phagocytic cells showed increased uptake with decreased nanoparticle size [21]. Yu *et al.* explored the size-dependent uptake of macrophage cells alone. Ultrasmall superparamagnetic iron oxide (uSPIOs) nanoparticles surrounded by PEG-poly(propylene sulfide) (PEG-PPS) were synthesized to be 30 nm, 40 nm, or 100 nm in diameter. As previously reported with polymeric nanoparticles, increased uSPIO size correlated with increased uptake by macrophage cells [22]. However, an *in vitro* study with macrophage cells resulted in the highest uptake at a diameter of 37 nm, which was not the largest size tested [9]. Currently, it is unclear if size-dependent uptake follows a different trend in macrophage cells than in nonphagocytic cells [5, 21, 22]. To develop a toolbox for designing nanoparticles that avoid the MPS, further studies are required to provide a more complete understanding of the effects of nanoparticle size on macrophage uptake.

Active Targeting

Nanoparticles are frequently coated with polyethylene glycol (PEG) to avoid the RES system and increase blood circulation half-life. The PEG coating makes the nanoparticle more hydrophilic and neutral, allowing them to bypass the immune system more easily; however, PEG poorly affects the cellular uptake and drug release [6, 23, 24]. Adding targeting ligands to the surface of a PEG-coated nanoparticle increases cellular uptake, helping to mitigate the uptake loss due to the initial PEG coating. The addition of targeting moieties improves the delivery process through active targeting of overexpressed antigens [25]. Surface ligands that bind to cellular receptors result in receptor-mediated uptake. A critical number of receptor-ligand interactions must occur to produce enough thermodynamic energy to overcome the resistive forces such as membrane elasticity and thermal fluctuations [26]. It is important to note that active targeting has drawbacks. Conjugating surface ligands to nanoparticles increases macrophage recognition and allows faster clearance compared to the non-targeted nanoparticles [24]. Active targeting can also create a binding site barrier effect, limiting nanoparticle penetration into the targeted tissue [27]. The *in vivo* drawbacks make it unclear if active targeting actually assists in the delivery process [27].

A possible solution to this problem is masking target ligands with a cleavable PEG-lipid conjugate. Masking the targeting ligands ensures ample circulation time while still utilizing active targeting [28]. In one study, nanoparticles targeted with folate receptor-targeted (FRT) liposomes were masked with a cysteine-cleavable 1,2-distearoyl-sn-glycero-3-phosphoethanolamine (DSP) - PEG coating were incubated with 9L glioma cells. Significant uptake was observed only in cells treated with cysteine [28]. Further *in*

vivo investigation revealed that the FRT masked nanoparticles did specifically target tumor cells after a cysteine injection and showed higher tumor cell uptake rates than nanoparticles without targeting liposomes, indicating the masking method is a promising solution to difficulties with active targeting [28].

To optimize active targeting via ligand density, Elias *et al.* conducted a study with HER2-targeted superparamagnetic iron oxide nanoparticles (SPIOs) on HER2/neu-positive (T6-17) cells. SPIOs were conjugated to HER2-affibodies previously ligated to an azido-fluorescent peptide (AzFP) at varying concentrations. 26 nm and 50 nm HER2-AzFP conjugated SPIOs were synthesized with different ligand densities. Both showed that the highest degree of cellular uptake occurs at a concentration of 0.01 ligands/nm squared [3]. The ligand-receptor binding energy also affects cellular uptake. Zhang *et al.* found that a smaller optimal radius and higher maximal cellular uptake is achieved with a larger ligand-receptor binding energy. Within the common range of typical antibody-antigen energies, the optimal radius can range from 25.4 nm to 30.2 nm [14].
Gold nanoparticles that are targeted to cancer cells show size-dependent cell binding [8]. When comparing 15 nm, 30 nm, 90 nm, and 150 nm targeted gold nanoparticles, the 15 nm diameter nanoparticles showed a 13-fold increase in cellular binding probability compared to the 150 nm diameter nanoparticles. However, 90 nm diameter cells showed optimal targeting in terms of gold mass per cell and surface area per cell [8]. While this indicates an optimal size range, additional studies should be conducted to evaluate the effects of size on targeting with differing parameters (e.g. varying cell lines, nanoparticle shapes, and core compositions).

Trends in vivo

While *in vitro* studies focus on individual aspects of the delivery process, *in vivo* studies shed light on the effects of nanoparticle size within the context of the body. Blood circulation half-life [6, 32, 33, 34], tumor permeability [7, 47, 34, 35], and biodistribution [4, 6, 32, 40] are all affected by the size of the nanoparticle. Table 2 provides a summary of several *in vivo* studies showing size-dependent trends.

Blood Circulation Half-Life

Once a foreign object enters a body, opsonization begins. Opsonin proteins attach to the foreign object and make it more visible to the mononuclear phagocytic system (MPS) [36]. A rapid MPS response results in the clearance of uncoated nanoparticles from the bloodstream within a few hours post-injection [4, 5, 32]. The rapid clearance of nanoparticles limited their use because nanoparticles do not have time to reach the targeted tissue [37]. Problems with avoiding the MPS have moved nanoparticles from the first generation of material design and biocompatibility to the second generation of stealth tactics and active targeting [1]. While some advances have increased circulation half-life ($t_{1/2}$), such as PEG coating [2, 6, 23, 24], a closer look at the basic size of a nanoparticle shows significant, size-dependent changes in $t_{1/2}$.

Some specific size limitations are known. A nanoparticle with a diameter less than approximately 10 nm will be rapidly eliminated by the kidneys [6, 38]. The reason for this clearance can be found by looking at each component of the kidney's filtration system. The kidney uses peritubular capillaries and renal corpuscles to filter the blood and produce urine. Within a renal corpuscle is the glomerulus, which has three layers

with varying pore sizes. The effective size cutoff of the overall structure is 10 nm [32]. The upper size limit of nanoparticles can vary based on the targeted cellular receptors [39], but a nanoparticle with a diameter greater than 200 nm will activate the complement system and be quickly removed from the blood stream, accumulating in the liver and spleen [2, 4, 33]. Moghimi *et al.* suggest a maximum size limit of 150 nm for spherical nanoparticles to avoid filtration in the spleen [40].

Further studies have narrowed the range of sizes and provided additional information about the effects of size on $t_{1/2}$. In a comparison between 24 nm and 37 nm shell cross-linked nanoparticles, the smaller particle had a higher retention at 10 minutes and at 4 hours post-injection. At 1 hour post-injection, 50% of the smaller nanoparticles were found in circulation, compared to only 5% of the larger nanoparticles [37]. A study with gold nanoparticles systematically tested the effects of nanoparticle size and mPEG weight on $t_{1/2}$. Five different nanoparticles, ranging from 17.72 nm to 86.73 nm, were each coated with mPEG 2 kDa, 5 kDa, and 10 kDa. The nanoparticles were injected into CD-1 mice, and $t_{1/2}$ was calculated from blood samples drawn at specific time intervals. For each size, $t_{1/2}$ increases as mPEG molecular weight increases. The greatest change is seen from mPEG 2 kDa to mPEG 5 kDa [34]. Between various core sizes, the smaller nanoparticles have a longer $t_{1/2}$. For example, there was an 8-fold increase in $t_{1/2}$ from the 86 nm core to the 17 nm core with the same coating [34]. Therefore, decreasing nanoparticle size and increasing the molecular weight of the PEG coating increases $t_{1/2}$ [6, 34].

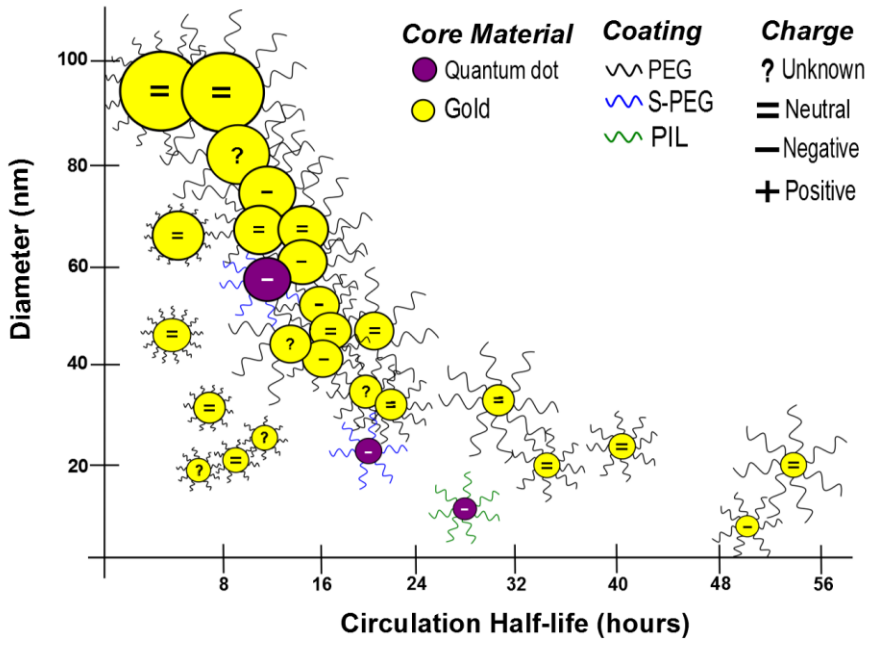

Figure 8: A schematic represents the relationship between nanoparticle size and circulation half-life.

As shown in Figure 8, each point represents a specific combination of characteristics that has been tested. Points are colored based on core material (yellow represents gold and purple represent quantum dots). The coating of the particle is shown by the lines surrounding each point. Black lines denote a PEG coating, with longer lines representing higher PEG molecular weight. Blue lines denote an S-PEG coating (silica shell with PEG5000 coating). Green lines denote a PIL coating. Within each point, surface charge is shown as positive (+), negative (-), neutral (=), or unknown (?).

Biodistribution

In vivo biodistribution of nanoparticles changes depending on nanoparticle properties and interactions with the living system [13]. In particular, nanoparticle size affects the biodistribution of nanoparticles throughout the body [6, 32, 33]. Particles on the micrometer scale remain in the body much longer than particles on the nanometer scale [33]. In one *in vivo* mouse model, micrometer particles remained in the spleen and the site of injection for at least two weeks, while nanoparticles of the same material were almost completely cleared in the same time frame [33]. The largest accumulations of nanoparticles typically occur in the blood, liver, and spleen [6]. Generally, larger nanoparticles accumulate in the liver and spleen more rapidly. There is still debate as to whether the rapid accumulation is due to simple filtration or increased binding opportunities between the MPS cells and the nanoparticles [36]. Examining the variations in biodistribution for 24 nm and 37 nm diameter shell cross-linked nanoparticles, smaller particles show a lower accumulation in the liver at 10 minutes post injection and lower kidney uptake at 4 hours post injection. Uptake in the spleen showed no correlation to size [37]. The minimum size to escape renal filtration, 10 nm, is illustrated by examining the biodistribution of spherical gold nanoparticles with diameters of 10 nm, 50 nm, 100 nm, and 250 nm at 24 hours post injection. The 50 nm diameter nanoparticle shows the lowest accumulation in both organs, but the 10 nm diameter nanoparticle shows the highest accumulation in the spleen and the liver [6]. In contrast, 15 nm, 50 nm, and 160 nm gold nanoparticles functionalized with PEG show decreasing accumulation from 50 nm to 15 nm [41].

Nanoparticle size impacts biodistribution within specific organs, as well as affecting the biodistribution throughout the body. The size-dependent distribution of nanoparticles is the result of various filters within organs or barriers between the organ and the surrounding fluid [4, 32]. For example, when nanoparticles from 20 nm to 100 nm in diameter were injected into the kidney tissue, no correlation between the particle size and particle accumulation was found in the peritubular capillaries. However, there was a strong correlation between particle size and particle accumulation in the renal corpuscles. Nanoparticles 50 nm in diameter accumulated in all renal corpuscle cells with decreasing quantities as the nanoparticle diameter approaches the extremes of the tested range [32]. An example of a barrier's impact can be found in a study that analyzed the effects of size when penetrating the blood-brain barrier. Nanoparticles between 25 nm and 500 nm were injected into rats; 3 hours post-injection, the biodistribution of nanoparticles in the brain tissue showed a strong correlation to nanoparticle size, with 25 nm particles showing the greatest accumulation [4].

In order to determine the effects of nanoparticle size on biodistribution, nanoparticle properties and biodistribution model parameter must be quantified [13]. A possible future method of evaluating the biodistribution of nanoparticles is a physiologically based pharmacokinetic model (PBPK) [13, 42]. PBPK models are discussed in further detail in the modeling section.

Pharmacokinetics of 6nm and 14nm SPIOs

We performed blood pharmacokinetic studies with several variations of the ^{64}Cu-SPIOs to understand the effect of size and PEG density. Both 6 nm and 14 nm iron cores

were prepared with chelator BAT, with and without targeting peptide. In addition the ratio of PEG to iron was increased in the first step of coating to increase the PEG density.

Particles were coated and characterized as shown in Figure 9. As shown, the size increased after coating with DSPE-PEG2k and the conjugation of VINP peptide. The surface charge was characterized with zeta potential. Sine maleimide group hydrolyzes, SPIOs have a negative charge before conjugation and the surface charge becomes more positive after conjugation of the VINP peptide.

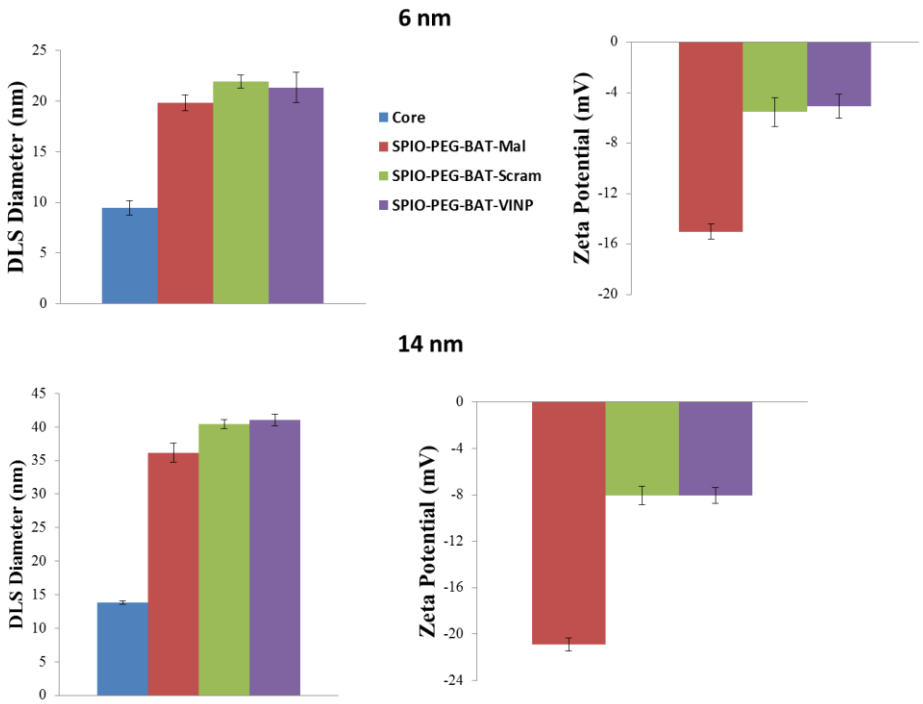

Figure 9: Characterization of 6 nm and 14 nm SPIOs using TEM, DLS diameter and zeta potential measurements.
The sized increased after coating with DSPE-PEG2k and post conjugation of VINP peptide. The zeta potential became less negative after conjugation of VINP peptide.

All animal procedures were performed in compliance with guidelines set forth by the Emory University Institutional Animal Care and Use Committee. Pharmacokinetics were validated after intravenous injection of 100 µg of 6nm and 14nm ^{64}Cu-SPIOs and ^{64}Cu-VINP-SPIOs in C57BL/6 (n=5 per time point) mice. Blood samples were collected 1min, 30min, 1 hour and 3 hour after injection in pre-weighed glass tubes. The weight of the blood was then measured and the amount of radioactivity was determined using a cobra counter.

The half-life of the contrast agent was determined by curve fitting to the equation:

$$N(t) = N_0 e^{-bt},\ T_{1/2} = \frac{\log(2)}{b},\ dT_{1/2} = \frac{(\log(2)db}{b^2}$$

N_0 referring to the initial amount of the contrast agent that decays; $N_{(t)}$ is the amount that still remains and has not yet decayed after a time t, $T_{1/2}$ is the half-life time of the decaying contrast agent, fitted value b is connected to half-life time $T_{1/2}$, db is the error of the fitted value b and $dT_{1/2}$ is the error of the half life time. Figure 10 shows the result of pharmacokinetic studies. The results show that the addition of the targeting peptide significantly decreases the blood circulation half-life in both 6 nm and 14 nm SPIOs. As the core size increases, blood circulation half-life decreases. Also, the increase in PEG density coating of the SPIOs, increases the blood circulation half-life. Based on these results, we selected the 14 nm targeted ^{64}Cu-SPIOs for tumor imaging and 6 nm ^{64}Cu-VINP-SPIOs for plaque imaging.

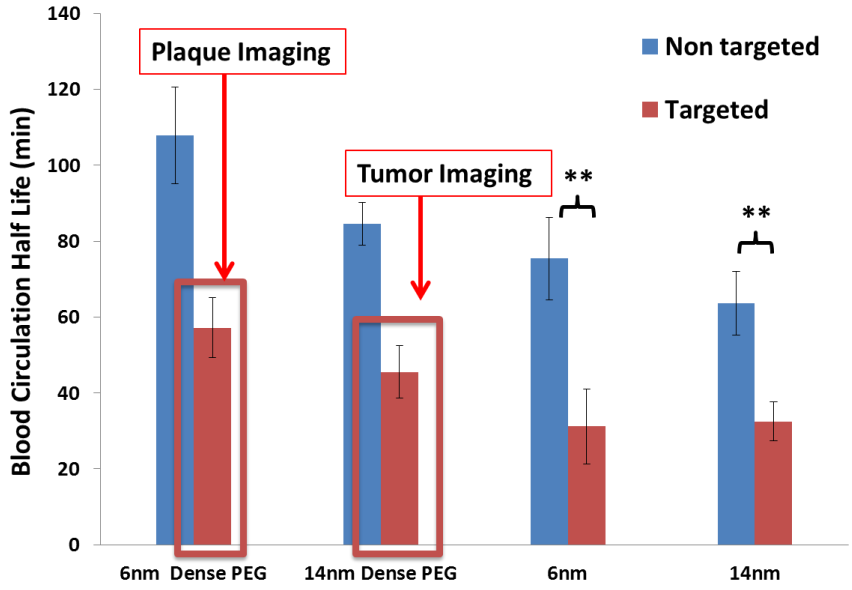

Figure 10: Blood circulation half-life of ^{64}Cu-VINP-SPIOs and ^{64}Cu-VINP-SPIOs with several variation of size and PEG density.
Higher PEG density increased the circulation half-life. The addition of targeting peptide significantly decreased the blood circulation half-life in both 6 nm and 14 nm. (**P<0.05)

To determine the biodistribution of 14 nm ^{64}Cu-SPIOs and ^{64}Cu-VINP-SPIOs, nanoparticles were administered via tail vein injection and accumulation in major organs was investigated. Groups of C57BL/6 mice (n=5 per time point) were sacrificed at 15min, 1 hr, 3 hrs, and 24 hrs post injection and select organs were weighed and measured with Cobra Counter for activity. A standard dose was prepared and measured to calculate the percent injected dose per gram (%ID/g). Data are expressed as percent injected dose per gram (%ID/g).

Biodistribution studies of 6 nm and 14 nm SPIOs

Initially, 14 nm SPIOs were prepared with 5% DSPE-PEG-amine and conjugated to DOTA-NHS according to Glaus et al. Biodistribution in female BALB/c mice was

performed and the results are shown in Figure 11. Blood circulation half-life is shorter as compared to the 14 nm SPIOs with chelator BAT.

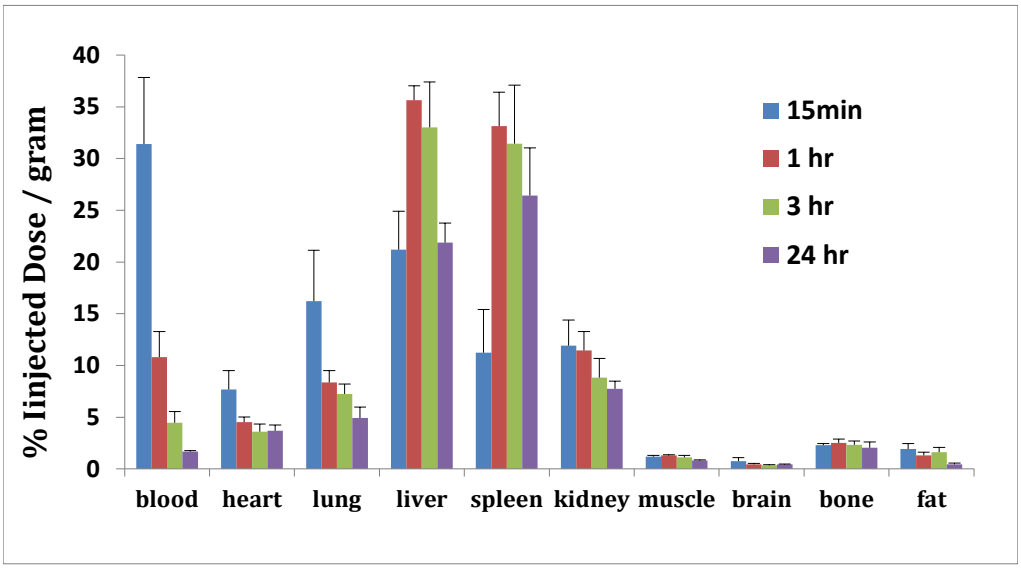

Figure 11: Biodistribution data of 14 nm Non-Targeted ^{64}Cu-DOTA-SPIO in Black C57 mice.

The following four figures show the biodistribution studies of 6 nm and 14 nm ^{64}Cu-VINP-SPIOs and ^{64}Cu-SPIOs. The particles were injected via retro-orbital injection in the following studies. As shown in Figure 12, %ID/g remains about 45% after 15 minutes and slowly drops to about 30% 1 hr post injection. The blood circulation half-life was calculated by curve fitting and it was found to be 107.9 minutes. The RES uptake was seen in the liver and spleen.

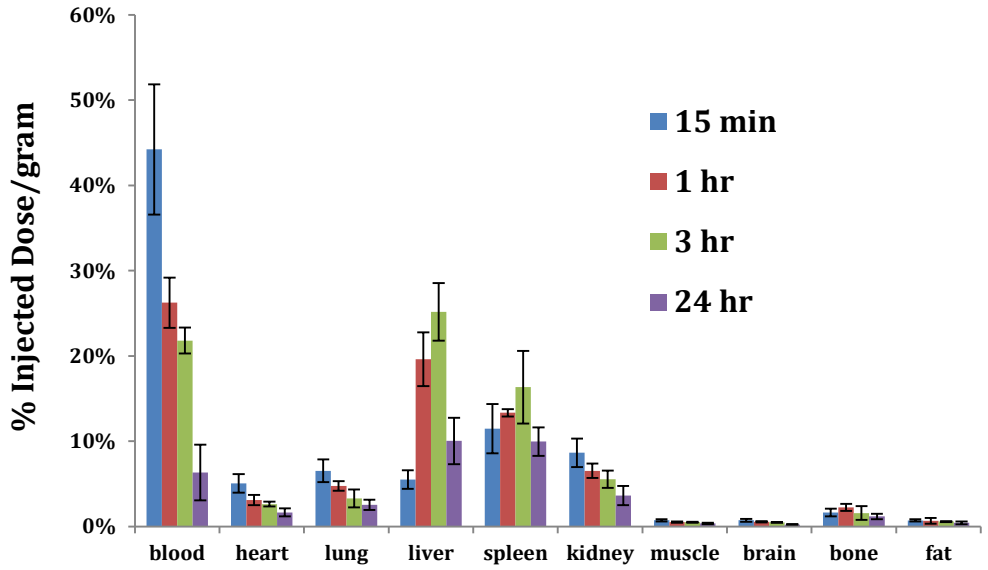

Figure 12: Biodistribution data of 6nm Non-Targeted ^{64}Cu-SPIO in black C57 mice.

To understand the effect of VINP targeting ligand on the nanoparticle biodistribution, the 6 nm ^{64}Cu-VINP-SPIOs was injected to C57 mice and the biodistribution studies was performed similar to the non-targeted 6 nm. As shown in Figure 13, the blood circulation half-life is about 26% 15 minutes post injection. The dose drops to about 10% after an hour. The blood circulation half-life was estimated to be about 31 minutes. It is important to note the increase in the dose in kidneys as compared to the non-targeted SPIOs. This increase may be due to the uptake of particles by mesangial cells within renal corpuscles.

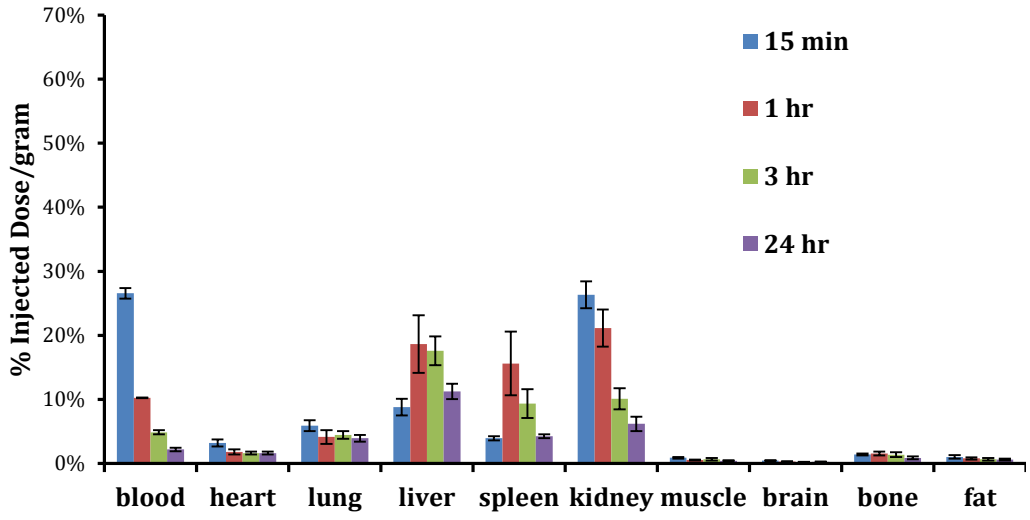

Figure 13: Biodistribution data of 6nm Targeted ^{64}Cu-SPIO in Black C57 mice.

To understand the effect of size on biodistribution, 14 nm ^{64}Cu-SPIOs were prepared. Figure 14 shows the biodistribution of 14 nm nanoparticles. The percentage remaining in the blood after 15 min was about 38% and declined over time to about 1% after 24 hours. The blood circulation half-life was calculated to be 84 minutes. The high uptake in the liver and spleen was expected. Compared to 6nm non-targeted SPIOs, the 14 nm had a lower circulation half-life.

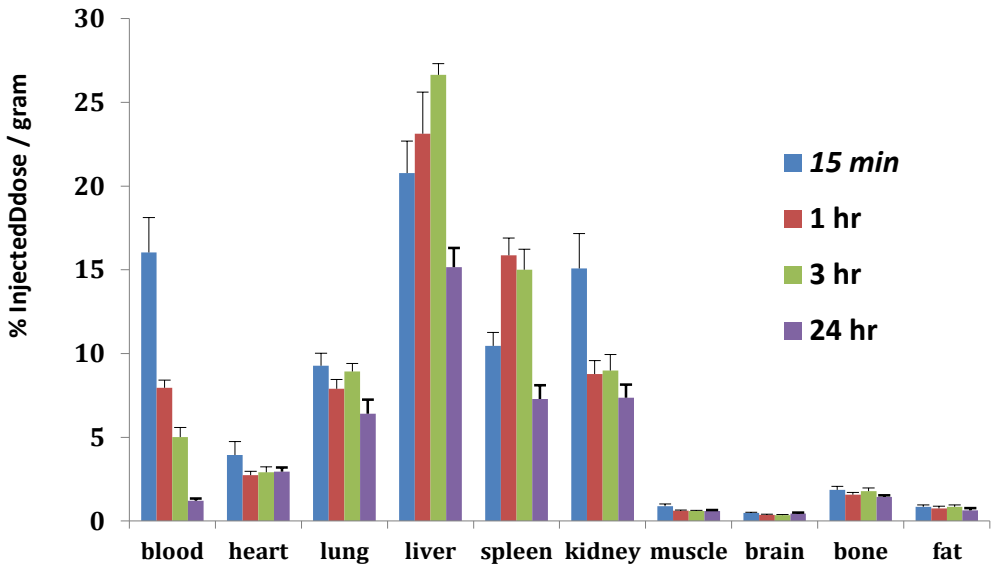

Figure 14: Biodistribution data of 14nm Non-Targeted ^{64}Cu-SPIO in Black C57 mice.

As shown in Figure 15, biodistribution was repeated with 14 nm targeted ^{64}Cu-VINP-SPIOs in black C57 mice. As it was seen in the case of 6 nm, the blood circulation half-life was decreased by addition of peptide targeting ligand. Liver and spleen had a very high uptake. The uptake in the kidneys was increased by addition of peptide which was similar to the 6 nm.

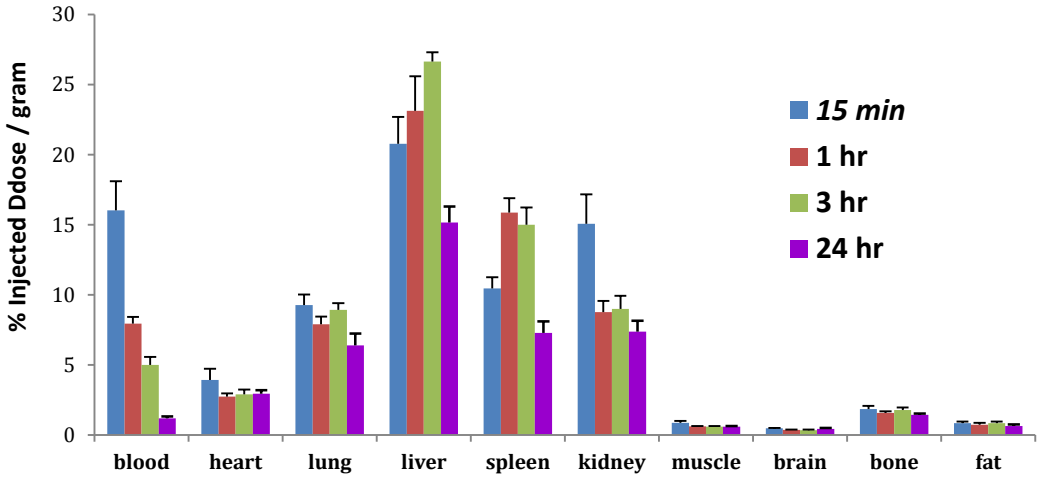

Figure 15: Biodistribution data of 14nm Targeted ^{64}Cu-SPIO in Black C57 mice.

Discussion and Conclusion

The effect of nanoparticle size and PEG density was investigated in a series of *in vivo* experiments. Several variations of nanoparticles sizes (6 nm and 14 nm) with and without peptide targeting was prepared and injected to mice. The results show that nanoparticle circulation half-life can be increased by the increase in PEG density. The size of nanoparticle also affects circulation half-life. 6nm SPIOs had higher circulation half-life compared to 14 nm SPIOs. Also, addition of targeting ligand decreases the blood circulation half-life. The addition of targeting ligand, causes a corona of proteins to develop on the surface of the SPIOs making it easier to be recognized by the inflammatory cells especially macrophages. Therefore, this leads to shorter circulation half-life. However, the increase in PEG density causes a conformational change from mushroom to brush chain conformation and forms a think hydrophilic layer at the surface. The hydrophilic layer creates a steric barrier which prevents the adsorption of opsonins and lipoproteins to the surface of the SPIOs. The increased PEG density makes

the SPIOs “invisible” to the reticulo-endothelial (RES) system, therefore prolonging their life time in the blood. This effect makes the SPIOs ideal vehicles for targeted imaging of tumor and plaque.

We believe that the increase in the kidney dose that was observed with the addition of the targeting peptide is a result of binding and disassembly by components of the renal filtration barrier.

The use of chelator BAT instead of DOTA causes the particle to clear the liver and spleen much faster. Based on these observations the 6 nm VINP-SPIOs with higher PEG density had the ideal blood circulation half-life for PET imaging of carotid ligation model. At the time, of these studies, we had determined that the focus of plaque imaging will be mainly on PET. Therefore, this particle with its long circulation half- life was mainly used to perform the imaging studies in the ligation model. The 14 nm CD105-SPIOs with higher PEG density was prepared for tumor imaging studies. The increase in core size from 6 nm to 14 nm significantly improves the MRI contrast, therefore, they would be more appropriate for MRI and PET studies.

References

1. Albanese A, Tang P, Chan WCW. The effect of nanoparticle size, shape, and surface chemistry on biological systems. *Annual Review of Biomedical Engineering*. 14, 1-16 (2012).

2. De Barros A, Tsourkas A, Saboury B, Cardoso V, Alavi A. Emerging role of radiolabeled nanoparticles as an effective diagnostic technique. *EJNMMI Research*. 2(1), 39-53 (2012).

3. Elias D, Poloukhtine A, Popik V, Tsourkas A. Effect of ligand density, receptor density, and nanoparticle size on cell targeting. *Nanomedicine: NBM*. 9(2), 194-201 (2013).

4. Kulkarni S, Feng S. Effects of particle size and surface modification on cellular uptake and biodistribution of polymeric nanoparticles for drug delivery. *Pharmaceutical Research*. 30(10), 2512-2522 (2013).

5. Liu X, Huang N, Li H, Jin Q, Ji J. Surface and size effects on cell interaction of gold nanoparticles with both phagocytic and nonphagocytic cells. *Langmuir*. 29, 9138-9148 (2013).

6. Dreaden E, Austin L, Mackey M, El-Sayed M. Size matters: gold nanoparticles in targeted cancer drug delivery. *Therapeutic Delivery*. 3(4), 457-478 (2012).**

7. Chauhan V, Stylianopoulos T, Martin J, *et al*. Normalization of tumour blood vessels improves the delivery of nanomedicines in a size-dependent manner. *Nature Nanotechnology*. 7(6), 383-388 (2012).

8. Peretz V, Motiei M, Sukenik C, Popovtzer R. The Effect of Nanoparticle Size on Cellular Binding Probability. *Journal of Atomic, Molecular, and Optical Physics*. 2012, 1-7 (2012).

9. Huang J, Bu L, Xie J, *et al*. Effects of nanoparticle size on cellular uptake and liver MRI with polyvinylpyrrolidone-coated iron oxide nanoparticles. *ACS Nano*. 4(12), 7151-7160 (2010).

10. Tong S, Hou S, Zheng Z, Zhou J, Bao G. Coating optimization of superparamagnetic iron oxide nanoparticles for high T2 relaxivity. *Nano Letters*. 10(11), 4607-4613 (2010).

11. Kucheryavy P, He J, John V, *et al*. Superparamagnetic iron oxide nanoparticles with variable size and an iron oxidation state as prospective imaging agents. *Langmuir*. 29(2), 710-716 (2013). **

12. Hobbs S, Monsky W, Yuan F, *et al.* Regulation of transport pathways in tumor vessels: role of tumor type and microenvironment. *Proceedings of the National Academy of Sciences of the United States of America.* 95(8), 4607-4612 (1998).

13. Li M, Al-Jamal K, Kostarelos K, Reineke J. Physiologically based pharmacokinetic modeling of nanoparticles. *ACS Nano*. 4(11), 6303-6317 (2010).

14. Zhang S, Li J, Lykotrafitis G, Bao G, Suresh S. Size-Dependent Endocytosis of Nanoparticles. *Advance Material*. 21, 419-424 (2009).

15. Lu F, Wu S, Hung Y, Mou CY. Size effect on cell uptake in well-suspended, uniform mesoporous silica nanoparticles. *Small*. 5(12), 1408-1413 (2009).

16. Jiang W, Kim B, Rutka J, Chan WCW. Nanoparticle-mediated cellular response is size-dependent. *Nature Nanotechnology*. 3(3), 145-150 (2008).

17. Karagoz B, Esser L, Duong H, Basuki Johan, Boyer C, Davis T. Polymerization-Induced Self Assembly (PISA) – control over the morphology of nanoparticles for drug delivery applications. *Polym. Chem*. (2014).

18. Niikura K, Matsunaga T, Suzuki T, *et al.* Gold Nanoparticles as a Vaccine Platform: Influence of Size and Shape on Immunological Responses *in Vitro* and *in Vivo*. *ACS Nano*. 7(5), 3926-3938 (2013).

19. Yuan H, Li J, Bao G, Zhang S. Variable Nanoparticle-Cell Adhesion Strength Regulates Cellular Uptake. *Physical Review Letters*. 105(13), (2010).*

20. Wang S, Lee C, Chiou A, Wei P. Size-dependent endocytosis of gold nanoparticles studied by three-dimensional mapping of plasmonic scattering images. *J. of Nanobiotechnology*. 8(1), 2010.

21. He C, Hu Y, Yin L, Tang C, Yin C. Effects of particle size and surface charge on cellular uptake and biodistribution of polymeric nanoparticles. *Biomaterials*. 31(13), 3657-3666 (2010).

22. Yu S, Lau C, Thomas S, *et al.* Size- and charge-dependent non-specific uptake of PEGylated nanoparticles by macrophages. *Int. J. Nanomedicine.* 7, 799-813 (2012).

23. Ruiz A, Salas G, Calero M, *et al*. Short-chain PEG molecules strongly bound to magnetic nanoparticle for MRI long circulating agents. *Acta Biomaterialia*. 9(5), 6421-6430 (2013).

24. Wang M, Thanou M. Targeting nanoparticles to cancer. *Pharmacological research: The Official Journal of the Italian Pharmacological Society*. 62(2), 90-99 (2010).

25. Salvati A, Pitek A, Monopoli M, *et al*. Transferrin-functionalized nanoparticles lose their targeting capabilities when a biomolecule corona adsorbs on the surface. *Nature Nanotechnology*. 8(2), 137-143 (2013).

26. Nel A, Madler L, Velegol D, *et al*. Understanding biophysicochemical interactions at the nano–bio interface. *Nature Materials*. 8, 543-557 (2009).

27. Lee H, Fonge H, Hoang B, Reilly R, Allen C. The Effects of Particle Size and Molecular Targeting on the Intratumoral and Subcellular Distribution of Polymeric Nanoparticles. *Mol. Pharmaceutics*. 7(4), 1195-1208 (2010).

28. McNeeley K, Karathanasis E, Annapragada A, Bellamkonda R. Masking and triggered unmasking of targeting ligands on nanocarriers to improve drug delivery to brain tumors. *Biomaterials*. 30, 3986-3995 (2009).

29. Brammer K, Oh S, Cobb C, Bjursten L, van der Heyde H, Jin S. Improved bone-forming functionality on diameter-controlled TiO(2) nanotube surface. *Acta Biomaterialia*. 5(8), 3215-3223 (2009).

30. Chithrani B, Ghazani A, Chan WCW. Determining the size and shape dependence of gold nanoparticle uptake into mammalian cells. *Nano Letters*. 6(4), 662-668 (2006).

31. Gamboa J, Leong K. In vitro and in vivo models for the study of oral delivery of nanoparticles. *Advanced Drug Delivery Reviews*. 65(6), 800-810 (2013).

32. Choi C, Zuckerman J, Webster P, Davis M. Targeting kidney mesangium by nanoparticles of defined size. *Proceedings of the National Academy of Sciences of the United States of America*. 108(16), 6656-6661 (2011).

33. Faraji A, Wipf P. Nanoparticles in cellular drug delivery. *Bioorganic & Medicinal Chemistry*. 17(8), 2950-2962 (2009).

34. Perrault S, Walkey C, Jennings T, Fischer H, Chan WCW. Mediating Tumor Targeting Efficiency of Nanoparticles Through Design. *NanoLetters*. 9(5), 1909-1915 (2009).

35. Hong H, Zhang Y, Sun J, Cai W. Molecular imaging and therapy of cancer with radiolabeled nanoparticles. *Nano Today*. 4(5), 339-413 (2009).

36. Owens D, Peppas N. Opsonization, biodistribution, and pharmacokinetics of polymeric nanoparticles. *International Journal of Pharmaceutics.* 307(1), 93-102 (2006).

37. Sun X, Rossin R, Turner J, *et al*. An Assessment of the Effects of Shell Crosslinked Nanoparticle Size, Core Composition, and Surface PEGylation on In Vivo Biodistribution. *Biomacromolecules*. 6(5), 2541-2554 (2005).

38. Zuckerman J, Choi C, Han H. Polycation-siRNA nanoparticles can disassemble at the kidney glomerular basement membrane. *Proceedings of the National Academy of Sciences of the United States of America*. 109(8), 3137-3142 (2012).

39. Bartlett D, Davis M. Physicochemical and biological characterization of targeted, nucleic acid-containing nanoparticles. *Bioconjugate Chemistry*. 18(2), 456-468 (2007).

40. Moghimi S, Hunter A, Andresen T. Factors controlling nanoparticle pharmacokinetics: an integrated analysis and perspective. *Annual review of pharmacology and toxicology*. 52, 481-503 (2012).

41. Terentyuk G, Maslyakova G, Suleymanova L, *et al.* Circulation and distribution of gold nanoparticles and induced alterations of tissue morphology at intravenous particle delivery. *J. Biophotonics*. 2(5), 292-302 (2009).

42. Li M, Panagi Z, Avgoustakis K, Reineke J. Physiologically based pharmacokinetic modeling of PLGA nanoparticles with varied mPEG content. *International Journal of Medicine*. 7, 1345-1356 (2012).

43. Pérez-Campaña C, Gómez-Vallejo V, Puigivila M, *et al.* Biodistribution of different sized nanoparticles assessed by positron emission tomography: a general strategy for direct activation of metal oxide particles. *ACS nano*. 7(4), 3498-3505 (2013).

44. Carmeliet P, Jain R. Molecular mechanisms and clinical applications of angiogenesis. *Nature*. 473(7347), 298-307 (2011).

45. Nagy J, Dvorak A, Dvorak H. VEGF-A and the induction of pathological angiogenesis. *Annu. Rev. Pathol. Mech. Dis.* 2, 251-275 (2007).

46. Fang J, Nakamura H, Maeda H. The EPR effect: Unique features of tumor blood vessels for drug delivery, factors involved, and limitations and augmentation of the effect. *Advanced Drug Delivery Review*. 63(3), 136-151 (2011).

47. Jain R, Stylianopoulos T. Delivering nanomedicine to solid tumors. *Nature Reviews Clinical Oncology.*7(11), 653-664 (2010).**

48. Stylianopoulos T, Soteriou K, Fukumura D, and Rakesh, PhD. Cationic nanoparticles have superior transvascular flux into solid tumors: insights from a mathematical model. *Annals of biomedical engineering.* 41(1), 68-77 (2013).

49. Popović Z, Liu W, Chauhan VP. A nanoparticle size series for in vivo fluorescence imaging. *Angewandte*. 49(46), 8649-8652 (2010).

50. Park J, Estrada A, Schwartz J, *et al.* Intra-organ biodistribution of gold nanoparticles using intrinsic two-photon-induced photoluminescence. *Lasers Surg. Med.* 42, 630-639 (2010).

51. Vlashi E, Kelderhouse L, Sturgis J, Low P. Effect of Folate-Targeted Nanoparticle Size on Their Rates of Penetration into Solid Tumors. *ACS Nano*. 7(10), 8573-8582 (2013).

52. Smith D, Simon J, Baker J. Applications of nanotechnology for immunology. *Nature reviews. Immunology.* 13(8) 592-605 (2013).

53. Park YM, Lee S, Kim Y, *et al*. Nanoparticle-Based Vaccine Delivery for Cancer Immunotherapy. *Immune network.* 13(5), 177-183 (2013).

54. Mottram P, Leong D, Crimeen-Irwin B, *et al*. Type 1 and 2 immunity following vaccination is influenced by nanoparticle size: formulation of a model vaccine for respiratory syncytial virus. *Mol. Pharm.* 4(1), 73-84 (2007).

55. Stano A, Nembrini C, Swartz M, Jeffrey A, Simeoni E. Nanoparticle size influences the magnitude and quality of mucosal immune respeonse after intranasal immunization. *Vaccine*. 30(52), 7541-7546 (2012).

56. Ahrens E, Bulte J. Tracking immune cells in vivo using magnetic resonance imaging. *Nature reviews. Immunology*. 13(10), 755-763 (2013).

CHAPTER 3

IN VIVO IMAGING OF EARLY STAGE ATHEROSCLEROTIC PLAQUES

Atherosclerosis

According to American Heart Association atherosclerosis is a leading cause of death in the United States. About 40% of the adult US population is at immediate risk of developing a cardiovascular disease, such as arthrosclerosis. Arthrosclerosis is a progressive inflammatory disorder characterized by lesions or fatty streaks that develop into plaque deposits with a high risk of rupture and thrombosis. Current imaging techniques, such as serum C-reactive protein, provide minimal data analysis that limits the assessment of cardiovascular risk [1,2,3].

Atherosclerosis is a gradual process caused by a combination of endothelial cell dysfunction, lipid oxidation, and lipid accumulation. As a result of endothelial cell activation, inflammation begins. Endothelial cells begin to secret adhesion molecules such as VCAM1 which will draw monocytes and lymphocytes into the arterial wall. Once monocytes transverse the endothelial barrier, they will differentiate into macrophages, take up lipids and become foam cells. Plaques usually go undetected and eventually develop into more insidious, life threatening fat deposits which could instigate myocardial infarction or sudden cardiac death. If caught early on, these plaque deposits are reversible by mobilizing the lesions and removing them from the vessel wall by a process called reverse cholesterol transport which involves a sequence of enzyme-mediated reactions[4- 6].

Once inflammation begins, the levels of C-reactive protein (CRP) which is a pentameric protein found in the blood plasma rises. Current techniques provide minimal data analysis that limits the assessment of cardiovascular risk. CRP is generally very low in healthy humans, however it significantly increases in patients with atherosclerosis even during the early stages of development [4- 6].

Figure 16 depicts the progression of atherosclerotic lesion and potential target for molecular imaging at each stage.

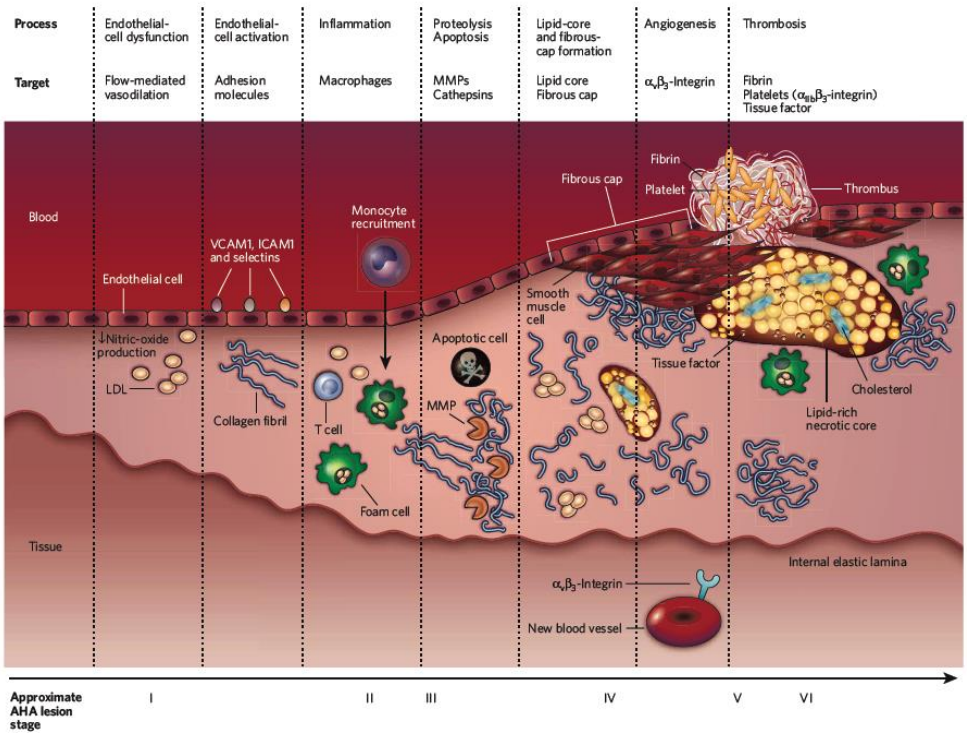

Figure 16: The progression of an atherosclerotic lesion [49].

VCAM1 Targeting

Vascular adhesion molecule-1 (VCAM-1) is present in active endothelial cells, macrophages, and smooth muscle cells (SMCs) and is upregulated in atherosclerosis due to inflammation. It contributes to the recruitment and adhesion of lymphocytes to

endothelial cells, forming plaque deposit [1, 7]. Currently, there are two developing techniques for detection: antibodies that bind to the surface of VCAM-1 expressing cells and expressing cells and specific peptides that are internalized by VCAM-1 expressing cells. Both methods have been studied extensively ex vivo as well as in vivo in order to determine which provides the most effective detection mechanism via magnetic resonance imaging (MRI). VINP linear peptide is shown to image atherosclerotic plaque in vivo. In this study, VINP peptide was conjugated to radio labeled SPIOs to image early stage plaque using PET and NIRF imaging, taking advantage of the nanoparticle long circulation half life and the superior sensitivity of PET imaging.

VCAM-1 specific antibodies have been used in association with nanoparticles and microbubbles to detect arthrosclerosis for MR imaging in previously established ex vivo and in vivo studies[8,9]. Ex vivo studies have shown that anti-VCAM-1 antibodies can be used to detect plaque, however, a low target-to-background ratio makes it difficult to differentiate lesions in *in vivo* mice models [3,10]. This is confirmed by in vivo studies conducted on apolipoprotein E-/- (apoE-/-) mice with surface modified anti-VCAM1 nanoparticles (VCAM-NPs) which were used to detect arthrosclerosis lesions via noninvasive MR imaging, however, at 1 hour most VCAM-NPs were still in circulation without clear signs of lesion receptor cell labeling. At 24 hours, accumulation of VCAM-NPs was faintly detected within the lesions. These low intensity signals might have been due to the dissociation of the anti-VCAM1 antibodies from the target caused by the low bond formation rate of antibodies. In rapid, high-shear circulation through vessels, contact time might not be adequate for antibody attachment to lesions [3, 11] . In order to

intensify these signals and improve the target-to-background ratio of MR imaging, a new approach was taken, cell internalization of VCAM-1 specific peptides.

A key advantage of VCAM-1 specific peptides is their capability to amplify signals through cellular internalization which improves uptake >12-fold in comparison to anti-VCAM-1 antibodies[1,12]. Ex vivo studies have been conducted with VCAM-1 specific peptide sequence surface modified nanoparticles (VNPs) in order to determine the specificity of the particle for arthrosclerosis lesions in endothelial cells. An 11-fold higher accumulation was seen in activated endothelial cells compared to other VCAM-1 expressing cells such as macrophages, thus suggesting that VNPs can be used to specifically target and detect arthrosclerosis[1,7]. Similar to the VCAM-NPs mice model, an in vivo study was conducted on apoE-/- mice via MRI to determine detection of lesions via peptide internalization. A change in signal intensity of MRI readings was detected with the accumulation of VNPs at arthrosclerosis regions which remained detectable for at least 24 hours [1, 7, 13]. This confirms that VNPs provide a more intensified detection of activated endothelial cells in comparison with VCAM-NPs in an *in vivo* model. VCAM-1 specific peptide sequences have also been used in *ex vivo* studies conducted on human carotid atheroma cells with a linear derivative of the cyclic peptide sequence used in Kelly et. al (VINP-28). This study suggests that VCAM-1 specific peptide sequences can be used in the future to detect arthrosclerosis in a clinical setting for humans. VINP-28 can also be used to tract the success of the arthrosclerosis treatment by detecting reductions in VCAM-1 expression as seen in apoE$^{-/-}$ mice with an atherogenic diet that were statin-treated to reduce plaque buildup in vessel walls [1, 7].

This noninvasive, progression methodology can be applied to a human model to track and analyze plaque development or depletion throughout the course of the disease.

Both techniques for arthrosclerosis detection have proven effective in *ex vivo* models, however, the long term goal is to transfer this detection method from cell lines and animal models to a human compatible model. VCAM-1 specific cell internalizing peptides have proved to be the better prospective for transitioning this dual modality imaging model due to its higher target-to-background ratio in mice models as well as its ability to remain detectable for longer periods of time. The VCAM-1 specific peptide sequences have also been successfully tested in an *ex vivo* human cell model which broadens the possibility for this to be applied *in vivo* for humans as well as opens up its applicability to help detect other diseases with their respective specified peptide sequences.

Plaque Imaging

Novel imaging techniques have been used for the evaluation and quantification of atherosclerosis plaque [14]. There are currently two leading clinical platforms: ^{18}F-fluorodeoxyglucose (^{18}FDG) imaging by PET and Ultrasmall superparamagnetic iron oxide (USPIO) nanoparticle-enhanced cardiac magnetic resonance (CMR) [15].

In a dual modality PET/CT study of 932 cancer patients, ^{18}FDG uptake was found to be a major predictor of future vascular events. In another study patients with cardio disease had a higher FDG uptake and a higher target-to-background ratio. There was a strong correlation between MMP-3 and MMP-9 and ^{18}FDG uptake and It was determined that inflammation and calcification did not overlap in the same arteries.

In a study to determine treatment of atheroma with atorvastatin, USPIOs were used as a marker to identify macrophage infiltration. Since USPIOs are phagocytosed by macrophages with a sufficient quantity, they were detected by MRI. The use of the USPIOs is important because macrophage infiltration is one of the leading risk factors for plaque rupture.

In a study by Weissleder, it was reported that VCAM-1 internalizing nanoparticle 28 VINP-28 has the highest affinity for endothelial cells and undergoes cell internalization to increase contrast via MRI. There was a high plaque target-to-background ratio for atherosclerosis. The VINP-28 was able to identified VCAM-1 expressing cells in human carotid artheromata. The macrophages may have enhanced the contrast of atherosclerosis because there are more macrophages present at the plaque then endothelial cells that express VCAM-1.

A second imaging technique is the contrast angiography that helps to visualize the plaque, however it is unable to view the entire arterial wall thus unable to identify changes in the disease such as alterations in wall thickness and plaque composition or volume. A third imaging technique is the intravascular ultrasound (IVUS) which is an invasive procedure that compensates for the angiography by allowing the diagnostician to view the progression of the plaque and the effects of drug therapy on the disease. An upcoming technique is computed tomography (CT) which is a minimally invasive procedure that accesses the wall thickening of arteries. Similar to the CT, high-resolution magnetic resonance imaging (MRI) can also be used as a noninvasive modality to monitor the plaque development, however both scans are very expensive to conduct on every potential patient [1,2,3,4, 16]. A more recent imaging technique is intravascular

optical coherence tomography (OCT) which is aimed at specific *in vivo* identification of vulnerable plaques. Although image artifacts inherent to the technique can lead to misclassification of pathology, OCT is the only technique able to detect eroded plaque thanks to its high spatial resolution [18].

In Vitro Targeting Studies

The yield of ^{64}CuSPIO radiolabeling was optimized by changing the coating to a combination of 95% DSPE-PEG methoxy, 5% DSPE-PEG maleimide and 2% lipid-PEG-BAT using the dual exchange solvent method. VCAM specific peptide was then conjugated to the SPIOs. *In vitro* studies with mouse endothelial cells revealed that the targeted SPIOs specifically target the VCAM1 on the surface of the cells about 5 fold more than the non-targeted SPIOs.

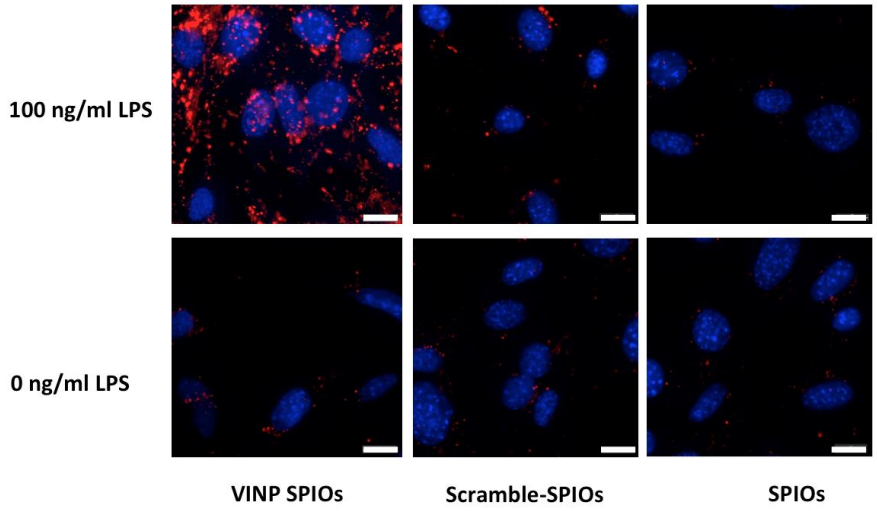

Figure 17: In vitro investigation of VINP-SPIOs with iMAECs. Scale bar = 10 µm Representative fluorescence images of immortalized mouse aortic endothelisal cells (iMAECs) stained with DiI labeled VINP-SPIOs, Scramble-SPIOs, or SPIOs after 1 hour incubation and subsequent washing with a 0 ng/mL and 100 ng/mL of LPS for 6 hours. (b) the bar graph shows the average ± standard deviation (n=3) for 6nm SPIOs. CTRL represents SPIOs without the targeting ligand. SCRAM repreents scrambled peptide SPIOs, VINP represents experimental SPIOs with VCAM-1 specific peptide. The p-values after performing t-tests that reached statistical significance ($p<0.05$) are indicated.

Figure 17 shows the representative fluorescence images of immortalized mouse aortic endothelial cells (iMAECs) stained with DiI labeled VINP-SPIOs, Scramble-SPIOs, or SPIOs after 1 hour incubation and subsequent washing with a 0 ng/mL and 100 ng/mL of LPS for 6 hours.

Phantom Studies

The PET imaging capability of 6nm ^{64}Cu-SPIOs and ^{64}Cu-VINP-SPIOs were analyzed using a 50 µCi sample on a Siemens invion microPET scanner. Radiolabeled nanoparticles were prepared in microcentrifuge tubes, placed in the scanner in an upright position and scanned for 10 minutes. Figure 18 shows the phantom image.

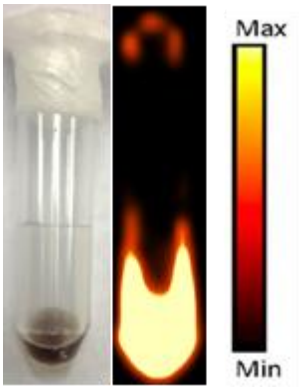

Figure 18: PhantomPET image of ^{64}Cu-VINP-SPIOs.

Carotid Ligation Model

All animal studies were carried out by procedures approved by the Emory University Institutional Animal Care and Use Committee (IACUC). ApoE$^{-/-}$ KO mice were obtained from Jackson Laboratories. All mice were fed a chow diet and water ad libitum. Male mice were ligated between 8 and 10 wk of age. Full ligation of LCA was carried out as previously described. Briefly, anesthesia was induced by inhaled isoflurane. Epilated area was disinfected with betadine, and a ventral midline incision (4–5 mm) was made in the neck. LCA was exposed by blunt dissection. LCA was ligated while the RCA was left intact. The incision was then closed with monofilament sutures. Mice were monitored until recovery in a chamber on a heating pad following surgery. Buprenorphine was given after ligation for pain relief. Figure 19 shows the schematic of the ligation and experimental procedure.

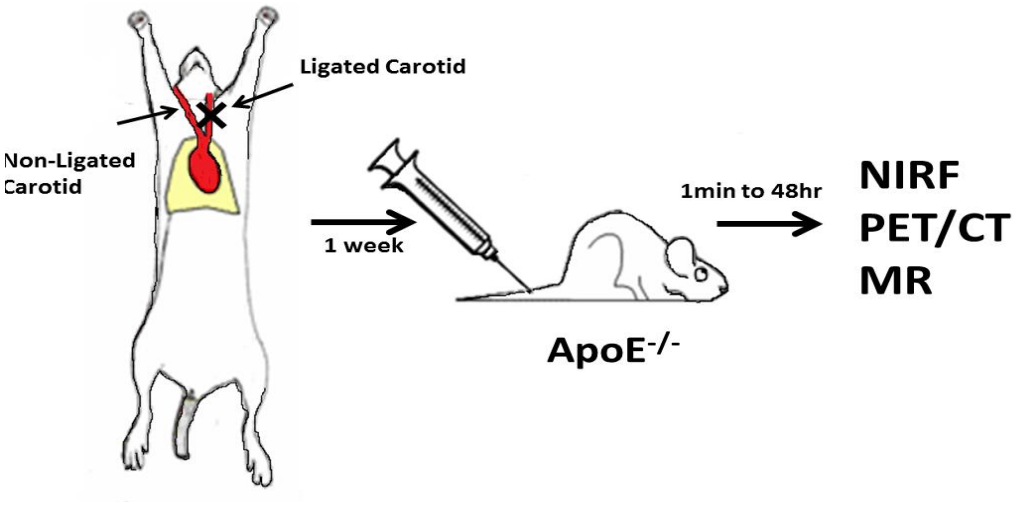

Figure 19: Carotid ligation model and experimental set up. Full ligation surgery was performed on ApoE$^{-/-}$ KO mice. 1 week post injection SPIOs were injected and imaging was performed.

In vivo and Ex vivo imaging using DiR labeled SPIOs

To optimize the imaging time, DiR labeled SPIOs were injected into ApoE$^{-/-}$ KO mice and imaged with in vivo near infrared imager 1hr, 2 hr, 3 hr, 4 hr, 6 hr and 24 hr post injection. Figure 18 shows the results of the experiment for the 24 hr time point.

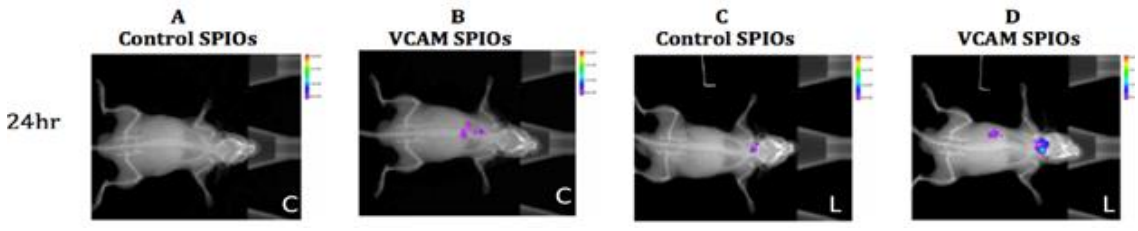

Figure 20: Representative in vivo NIRF imaging of carotid ligation black C57 mice.

Figure 20 shows Representative *in vivo* NIR imaging with A) control ApoE$^{-/-}$ KO mice and unconjugated SPIOs (n=2), B) control ApoE$^{-/-}$ KO mice and VCAM peptide conjugated SPIOs (n=2) C) unconjugated SPIOs injected to carotid ligated ApoE$^{-/-}$ KO mice 7 days post surgery (n=2) D) VCAM peptide conjugated SPIOs injected to carotid ligated APO KO mice (n=2). NIR images show the inflammation site with targeted SPIOs much better than the control SPIOs. (L-Ligation model, C-Control). To further quantify the targeting efficiency of VCAM-targeted SPIOs compared to control SPIOs, left and right carotids were excised and imaged at 24 hr time point. As shown in Figure 21, *ex vivo* carotid artery analysis was performed with A) non conjugated control SPIOs on control mice (n=2), B) VCAM-SPIOs on control mice (n=2) and C) VCAM-SPIOs on ligation mice (n=2). (surgical ligation performed on left carotid, L-left, C-control). Targeted SPIOs accumulate at the site of inflammation (L) over 5 folds compared to the control (C).

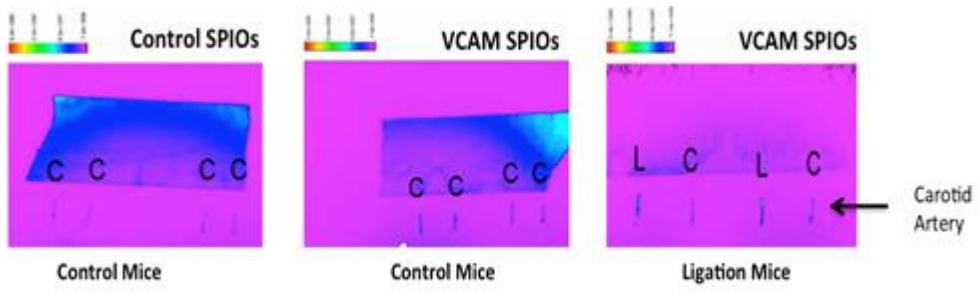

Figure 21: Ex vivo carotid artery analysis SPIOs.
Ex vivo carotid artery analysis was performed with non-conjugated control SPIOs on control mice (n=2), VCAM-SPIOs on control mice (n=2) and VCAM-SPIOs on ligation mice (n=2). (Surgical ligation performed on left carotid, L-left, C-control).

In vivo PET/CT imaging using ^{64}Cu-VINP-SPIOs

MicroPET scans were performed using a microPET Focus 120 (Siemens Medical Solutions USA, Inc., Malvern, PA). C57/bl mice with carotid ligation were given tail vein injections with 50 μCi of ^{64}Cu-VINP-SPIOs or ^{64}Cu-scramble-SPIOs (0.1 mg Fe/kg body weight) in 100 μL PBS. The peptide sequence used as scramble is Anatomical information was obtained from CT scans (microCAT II, Siemens Medical Solutions USA, Inc., Malvern, PA) performed immediately after completion of microPET. Analysis of microPET images was accomplished using vendor software (ASIPro, Siemens Medical Solutions USA, Inc.) on decay-corrected images. Coregistration of microPET and microCT images was performed by Inveon Software package. Figure 22 shows the co-registered microPET-microCT of C57bl mice with ligation on left carotid administered 50 μCi of ^{64}Cu-BAT-VINP-SPIO (10 mgFe/kg body weight, 100 μl injection volume). PET imaging of carotid ligation mouse model shows that VINP-^{64}Cu-SPIOs accumulated more in the ligated left carotid compared to the right.

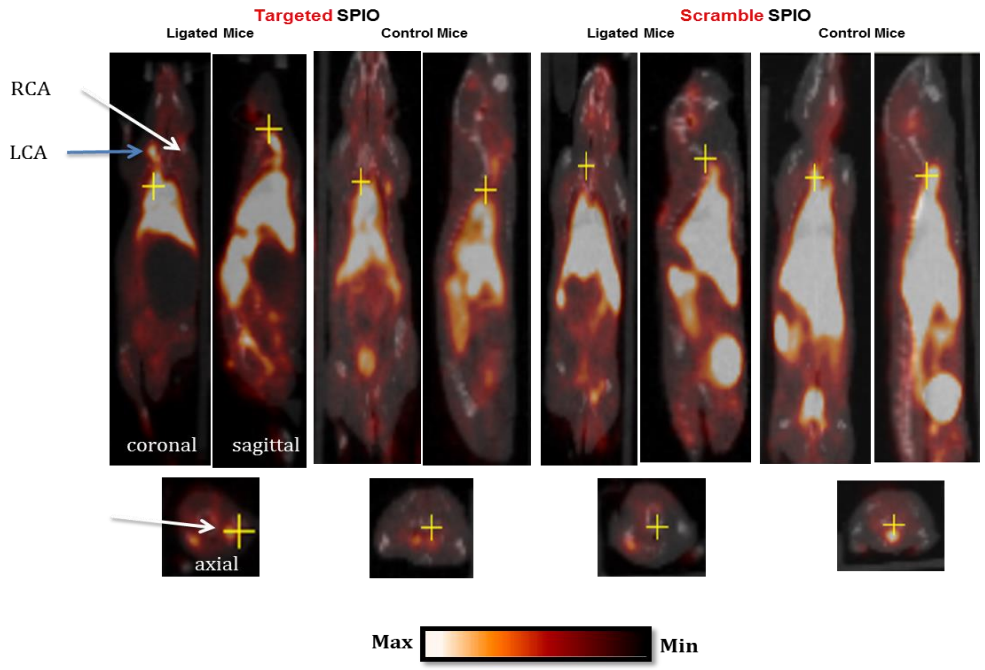

Figure 22: microPET/microCT images of inflammation in carotid ligation APO/E$^{-/-}$ KO mice with targeted SPIOs.
Co-registered microPET-microCT of C57bl mice with ligation on left carotid administered 50 µCi of 64Cu-BAT-VINP-SPIO (10 mgFe/kg body weight, 100 µl injection volume).

The results of quantitative image analysis of PET signal due to SPIO accumulation in Left Carotid Artery (LCA, ligated) versus Right Carotid Artery (RCA, control) are shown in Figure 23. A region of interest was selected as the LCA and the standard uptake values (SUVs) were normalized by that at LCA to give the normalized PET signal.

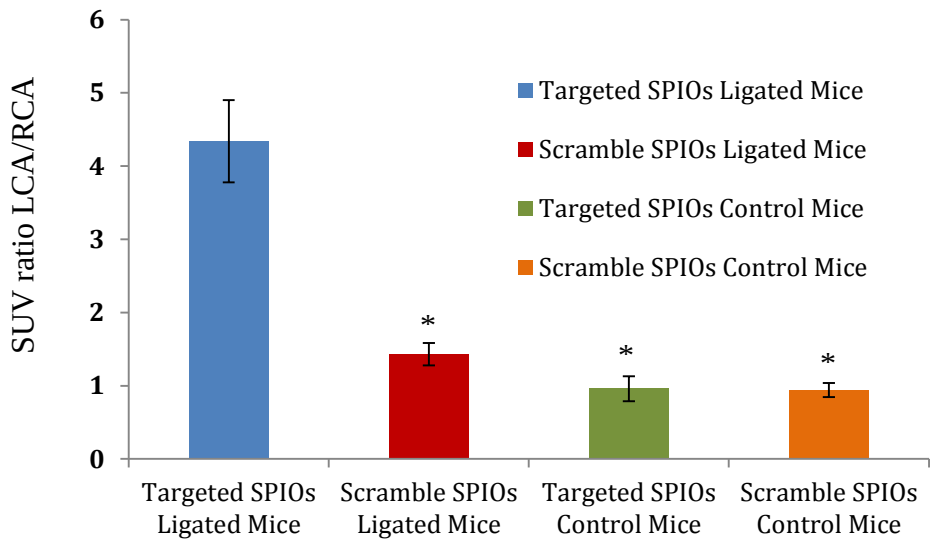

Figure 23: Quantitative image analysis of accumulation of SPIOs in Left Carotid Artery (LCA) versus Right Carotid Artery (RCA).
A region of interest was selected as the LCA and the standard uptake values (SUVs) were normalized to LCA. The difference between the targeted SPIOs and other control groups were statistically significant ($p<0.05$)

PET/CT imaging of carotid ligation mouse model shows that VINP-^{64}Cu-SPIOs accumulated more in the ligated left carotid compared to the right. Quantitative image analysis shows that the LCA over RCA ratio is about 2 fold higher when targeted SPIOs were tested in carotid ligation mode. Scramble-^{64}Cu-SPIOs were used as a control in the ligation and control mice. The difference between the targeted SPIOs and other control groups were statistically significant ($p<0.05$).

Discussion and Conclusion

We have developed a multimodality nanoparticle-based contrast agent by integrating near-infrared dye DiR into the coating of ^{64}Cu-SPIOs probes, and performed circulation half-life and biodistribution measurements. These probes were used in

imaging studies of inflammation with a carotid ligation mouse model. Specifically, SPIOs of 6 nm were coated with amphiphilic DSPE-PEG copolymer using a dual solvent exchange method. PEG molecules with amine and maleimide functional groups were incorporated in the coating for radiolabeling and targeting. These SPIOs were radiolabeled using ^{64}Cu and conjugated with peptides (VINP) targeting VCAM-1. To determine the serum stability of ^{64}Cu VINP-SPIOs, nanoparticles were incubated with mouse serum at 37^{o}C and analyzed using radio-FPLC. The pharmacokinetics and biodistribution of ^{64}Cu-SPIOs (non-targeted) and ^{64}Cu-VINP-SPIOs were evaluated in vivo. Vessel wall inflammation was induced in murine carotid arteries through full ligation of left carotid artery (LCA). Carotid ligated mice were given tail vein injections with 50 μCi of ^{64}Cu-

VINP-SPIOs as targeted probes or ^{64}Cu-scramble-SPIOs as control probes (0.1 mg Fe/kg body weight) in 100 μL PBS. PET/CT imaging was performed 4 hr post tail-vein injection of ^{64}Cu-VINP-SPIOs. Anatomical information was obtained from CT scans. PET imaging of carotid ligation mouse model showed that the ^{64}Cu-VINP-SPIOs had a much higher accumulation more in the ligated left carotid compared to the right (control, no ligation). This accumulation could be due to mechanical restraining of the left carotid compared to right. But, the use of scramble conjugated SPIOs and non-targeted SPIOs showed that mechanical narrowing of the artery increases the LCA to RCA ratio for scramble. But, this increase is more than 2 folds when using the VINP peptide conjugated SPIOs.

Quantitative image analysis indicates that the LCA over RCA ratio is about 4 fold higher when targeted SPIOs were used in carotid ligation mode, as shown in Figure 1.

Our results clearly indicate that the ^{64}Cu-VINP-SPIOs can be used to image inflammation with PET with high specificity and sensitivity. Both fluorescence imaging and MRI were also performed with carotid ligated mice and the results confirmed the PET imaging result.

A potential challenge with the use of this nanoparticle is the increase in false positive. Since VCAM1 can be overexpressed due to inflammation, the nanoparticles targeted with VINP could detect any type of inflammation not just the ones leading to plaque development. Therefore, there is a need to find an ideal target that is specific to plaque. Inflammatory makers such as hs-CRP, interleukins 6, 10 and 18, soluble CD40 ligand, P- and E-selectin, NT-proBNP, fibrinogen and cystatin C have shown limited success when used by themselves. But the combination of fibrinogen and NT-proBNP contained predictive information in addition to clinical parameters. In the future we suggest to target multiple markers to provide clinicians with predictive information [44].

References

1. R. Rossin, S. Muro, M. J. Welch, V. R. Muzykantov, and D. P. Schuster, "In vivo imaging of 64Cu-labeled polymer nanoparticles targeted to the lung endothelium.," *J. Nucl. Med.*, vol. 49, no. 1, pp. 103–11, Jan. 2008.

2. K. a Kelly, J. R. Allport, A. Tsourkas, V. R. Shinde-Patil, L. Josephson, and R. Weissleder, "Detection of vascular adhesion molecule-1 expression using a novel multimodal nanoparticle.," *Circ. Res.*, vol. 96, no. 3, pp. 327–36, Feb. 2005.

3. P. L. Nahrendorf, M., J.R. McCarthy, "Over a Hump for Imaging Atherosclerosis Nanobodies Visualize Vascular Cell Adhesion Molecule-1 in Inflamed Plaque.," *Circ. Res.*, vol. 110, no. 7, pp. 902–903, 2012.

4. B. A. Kaufmann, "Molecular imaging of inflammation in atherosclerosis with targeted ultrasound detection of vascular cell adhesion molecule-1," *Circulation*, vol. 116, no. 3, pp. 276–284, 2007.

5. P. P. Toth, "Atherosclerosis: The Underlying Disease.," *J. Fam. Pract.*, vol. 58, no. 11, 2009.

6. M. Crowther, “Pathogenesis of Atherosclerosis,” *Am. Soc. Hematol.*, 2005.

7. E. a Osborn and F. a Jaffer, “The year in molecular imaging.,” *JACC. Cardiovasc. Imaging*, vol. 3, no. 11, pp. 1181–95, Nov. 2010.

8. M. Nahrendorf, F. a Jaffer, K. a Kelly, D. E. Sosnovik, E. Aikawa, P. Libby, and R. Weissleder, “Noninvasive vascular cell adhesion molecule-1 imaging identifies inflammatory activation of cells in atherosclerosis.,” *Circulation*, vol. 114, no. 14, pp. 1504–11, Oct. 2006.

9. K. Iiyama, “Patterns of vascular cell adhesion molecule-1 and intercellular adhesion molecule-1 expression in rabbit and mouse atherosclerotic lesions and at sites predisposed to lesion formation.,” *Circ. Res., vol. 85, no. 2, pp. 199–207, 1999.*

10. P. Caravan, J. J. Ellison, T. J. McMurry, and R. B. Lauffer, “Gadolinium(III) Chelates as MRI Contrast Agents: Structure, Dynamics, and Applications.,” *Chem. Rev.*, vol. 99, no. 9, pp. 2293–352, Sep. 1999.

11. A. Tsourkas, “In Vivo Imaging of Activated Endothelium Using an Anti-VCAM-1 Magnetooptical Probe,” *Bioconjug. Chem.*, vol. 16, no. 3, pp. 576–581, 2005.

12. R. W. Jaffer, F.A., P. Libby, “Molecular and cellular imaging of atherosclerosis - Emerging applications,” *J. Am. Coll. Cardiol.*, vol. 47, no. 7, pp. 1328–1338, 2006.

13. M. Nahrendorf, “F-18-4V for PET-CT Imaging of VCAM-1 Expression in Atherosclerosis,” *Jacc-Cardiovascular Imaging*, vol. 2, no. 10, pp. 1213–1222, 2009.

14. R. Southworth, “Renal vascular inflammation induced by Western diet in ApoE-null mice quantified by F-19 NMR of VCAM-1 targeted nanobeacons,” *Nanomedicine-Nanotechnology Biol*. Med., vol. 5, no. 3, pp. 359–367, 2009.

15. D. E. Owens, “Imaging of Atherosclerosis,” *Annu. Rev. Med.*, vol. 62, no. 1, pp. 25–40, 2011.

16. N. Savita, S. Maitra, and U. Ravishankar, “Multimodality Molecular Imaging – An Overview With Special Focus on PET/CT,” *Apollo Med.*, vol. 7, no. 3, pp. 190–199, Sep. 2010.

17. Z. A. F. Javier Sanz, “Imaging of atherosclerotic cardiovascular disease,” *Nature, vol*. 451, pp. 953–957, 2008.

18. Kaski JC, Fernandez-Berges DJ, Consuegra-Sanchez L, et al. “A comparative study of biomarkers for risk prediction in acute coronary syndrome-Results of the SIESTA (Systemic Inflammation Evaluation in non-ST-elevation Acute coronary syndrome) study,” *Atherosclerosis*. 2010;212(2):636–43

CHAPTER 4

IN VIVO TUMOR IMAGING

Cancer is responsible for one-fourth of deaths in the United States. In 2014, it is expected that 1,665,540 people will develop cancer in the United States alone. Of these new cases, 235,030 individuals are expected to develop breast cancer [27]. Breast cancer growth and metastasis, like other tumors, both depend on the tumor's capability to rapidly form new blood vessels through angiogenesis [2,3].This process begins early in tumor development, with tumors smaller than 0.2 mm already showing the presence of angiogenesis [20]. As a tumor grows, oxygen and other necessary nutrients become scarce due to their limited diffusive nature. Tumor cells are forced to adapt to a hypoxic environment. In this environment, there is an upregulation of hypoxia inducible factor-1 (HIF-1) which signals cell survival by promoting angiogenesis, thus signaling the production of angiogenic factors such as vascular endothelial growth factor (VEGF), fibroblast growth factor (FGF), and endoglin (CD105) [21]. Tumor imaging with many types imaging modalities has been widely studied, however, the most sensitive imaging modality is PET imaging compared to existing non invasive diagnostic imaging modalities such as US, MR and CT [22]. Because of its superior sensitivity, PET imaging is now the standard procedure for cancer diagnosis [23]. However, there are limitations with ^{18}FDG PET imaging for cancer diagnosis: Low level of ^{18}FDG avidity in some malignancies such as primary adenocarcinoma of the lung that manifests as a subsolid nodule and in primary carcinoid tumors of the lung can lead to misinterpretation of PET studies and altered diagnosis. To overcome the potential limitations of ^{18}FDG-PET in the

diagnosis, there is a need for the development of PET imaging agents to interrogate different metabolic pathways, receptors or targets [8-9].

In vivo imaging of 4T1 Tumor

Developing therapeutic approaches are focusing on antiangiogenic treatments that use vascular targeting to selectively inhibit or destroy the tumor vasculature while maintaining normal blood flow in healthy tissue [2,3-10]. Nanoparticle-based molecular imaging is also focusing on angiogenic biomarkers because targeting the tumor vasculature reduces the needed blood circulation half-life of the nanoparticles and thus decreases background signal [27]. Additional benefits of vascular targeting for both imaging and therapy include easy access to target cells, low risk of antigen-negative cells, no requirement of extravasation, and universal targets for numerous solid tumors [10-12]. While no tumor vasculature-specific marker has been found, targets for therapeutic and diagnostic applications are emerging based on the unique characteristics of the tumor vasculature [18]. Tumor endothelial cells undergo hypoxic stress and rapid proliferation, which results in the up-regulation of some proteins that may be used as targets [29]. Vascular targeting shows promise for improving diagnostics and therapeutics for many solid tumors [2,10,12]. By studying the factors for tumor growth and the characteristics of the tumor environment, possible vascular targets have been found from up-regulated proteins [10-13].

Several VEGF targeting drugs have been approved for cancer treatment [0]. By 2007, three direct inhibitors of VEGF were approved for therapy. However, the treatments have not shown increased survival rates in all patients. It is possible that disease progression may be continuing along different angiogenic pathways even after

anti-VEGF therapy, which justifies the need to further explore other vascular targets for tumor therapy and diagnostics [25].

CD105, or endoglin, is a transmembrane glycoprotein overexpressed in endothelial cells undergoing angiogenesis and up-regulated by hypoxia [3,16,17]. The expression level of CD105 correlates with poor prognosis in more than ten different solid tumor types, making it a promising universal target for solid tumor prognostic, diagnostic, and therapeutic applications [12,18,20]. Since CD105 is not detectable in resting endothelial cells, it is a prime vascular target for antiangiogenic diagnostics [28]. Currently, immunohistochemistry of CD105 is a standard approach for determining tumor microvessel density [30]. Research studies of nanoparticles conjugated to anti-CD105 antibodies seek to use CD105 as a target for future drug delivery and imaging applications [22]. Previously, both graphene and mesoporous silica cores were conjugated to an anti-CD105 antibody. With both core types, *in vitro* experiments showed that CD105 served as an effective vascular target for angiogenic endothelial cells. For *in vivo* studies, a mouse 4T1 tumor model was used. The 4T1 tumor model can metastasize similar to human breast cancer and thus accurately represents the late stages of cancer [12,18,21]. In mice with 4T1 breast cancer tumors, ^{64}Cu labelled nanoparticles conjugated to anti-CD105 antibodies demonstrated CD105-specific tumor uptake. PET scans of the mice confirmed the increased tumor uptake for both graphene and mesoporous silica cores when CD105 targeting was added.[12, 18] Imaging studies have sought to create CD105-specific agents for PET and NIRF. Initial *in vitro* studies showed that labeling anti-CD105 antibodies with NIRF dye and ^{64}Cu did not affect the antibody binding affinity. Serial *in vivo* PET/NIRF images showed that image contrast and 4T1

tumor uptake with CD105 targeting were superior than the contrast and uptake seen in passive targeting [30]. In another study, liposomes conjugated to anti-CD105 antibodies also helped to enhanced MR imaging [22]. Some anti-CD105 antibodies have already moved into clinical trials. TRC105, a monoclonal antibody that binds to CD105, underwent its first-in-human clinical trial beginning in January 2008 and has completed five clinical studies. TRC105 is well-tolerated at clinically relevant doses and may be combined with VEGF inhibitors [20].

Currently, the most commonly used technique for cancer detection is X-ray imaging to detect abnormal masses or microcalcifications in the body; however, further invasive endoscopic catheter-based scans and biopsies need to be conducted in order to confirm the presence of a benign or malignant tumor, as well as determine its staging [24]. Due to the limited data assessment capabilities of current diagnostics and the invasiveness of these procedures, a novel, noninvasive imaging technique needs to be developed that will provide physicians with a complete prognosis of the developing tumor as well as allow tracking of the tumor overtime.

In recent years, investigation into new multimodal nanoparticles and imaging techniques has begun. Theranostic nanoparticles, which use the same nanoparticles for imaging and therapeutic delivery, have been explored. Combining therapy and imaging increases cost and synthesis complexity [25]. However, CD105 could be used as a theranostic target due to the promise of vascular targeting in imaging applications and antiangiogenic therapy. Shifting to imaging modalities, multimodal imaging techniques such as PET/CT have been used successfully in clinical applications since the 1990's [26]. PET imaging is highly sensitive and quantitative but has low spatial resolution [27].

CT provides the anatomical context for the PET scan. However, MRI may serve as a better anatomic imaging modality than CT especially in soft tissues. A PET/MRI combination would allow for an anatomic MR context, functional MR measurement, and PET molecular imaging of tumors [26]. MRI is also advantageous over CT because it uses no ionizing radiation and has superior soft tissue contrast [28]. Nanoparticles are useful as imaging probes because of their physicochemical properties, small size, lack of toxicity, ease of functionalization, and high surface area to volume ratio [29]. In particular, superparamagnetic iron oxide nanoparticles (SPIOs) have shown promise as an MR contrast agent in the past because the SPIOs create a strong localized magnetic field disturbance that causes strong negative contrast [28]. Functionalizing SPIOs with targeting moieties for specific cellular markers aids in highlighting disease sites [30]. For example, $\alpha_v\beta_3$ integrin–targeted ultrasmall SPIOs decreased T_2 relaxivity and increased negative contrast of tumors more effectively than plain particles [31]. SPIOs radiolabelled with ^{64}Cu, a positron-emitting radionuclide, produced strong MR and PET signals and showed high blood retention at early time points post-injection [28]. Despite the promising results from initial CD105 targeting experimentation using ^{64}Cu labeled nanoparticles, few studies have been conducted with CD105 as a target. Radiolabeled nanoparticles conjugated to anti-CD105 antibodies can further enhance diagnostic and prognostic imaging for tumors by highlighting the tumor vasculature, as well as provide a universal contrast agent. The development of an agent targeting CD105 that can be used in PET/MR multimodal imaging would allow for significantly improved diagnostics. This study focuses on the *in vitro* cellular uptake and *in vivo* molecular imaging of anti-CD105 antibodies conjugated to SPIOs. Herein, we report the synthesis and application

of a uniform CD105 targeted MRI/PET contrast agent against the in vitro and in vivo growth of 4T1 tumor cell line.

Surface coating and functionalizing ^{64}Cu-CD105 Targeted SPIOs

The SPIOs were functionalized with carboxy groups and ^{64}Cu-specific chelators. The ^{64}Cu-specific chelator, 6-[*p*-(bromoacetamido)benzyl]-1,4,8,11-tetraazacyclotetradecane-*N*,*N*′,*N*″,*N*‴-tetraacetic acid (BAT), was conjugated with an artificial lipid to form a BAT-PEG-lipid. The SPIOs were made water soluble via a dual solvent exchange method. Initially, 6 nm and 14 nm SPIOs and a PEG solution of 88% DSPE-PEG(2000)Methoxy (10mg/mL), 2% BAT-PEG-lipid, and 10% DSPE-PEG(2000)Carboxy (5mg/mL) were mixed at varying weight ratio (1:8 for 6nm and 1:4 for 14nm). Chloroform was added at 4 times the volume of SPIOs minus the volumes of DSPE-PEG(2000). Finally, DMSO was gradually added at 4 times the total volume of the contents of the flask. The mixture was left to react for 1 hour before evaporating 20% of the DMSO via a vacuum pump. All the flasks were oven-dried overnight and washed with chloroform three times before use. All experiments were conducted in a dry box (104.7ppm O_2, 7.5ppm H_2O, and 4.4mbar pressure).

After the first solvent exchange, the SPIOs were made water soluble by gradually mixing the SPIO solution with water at a 1:5 volume ratio. The solution was filtered to remove the empty micelles via 3 rounds of centrifuge (100K Da cutoff size filters) at 25,000 rcf for 20 minutes and 3 rounds of ultracentrifuge at 80,000 rcf for 50 minutes (6nm) and 65,000 rcf for 50 minutes (14nm), both at 4˚C. The SPIOs were then filtered with a 2μm syringe-filter to remove any aggregates.

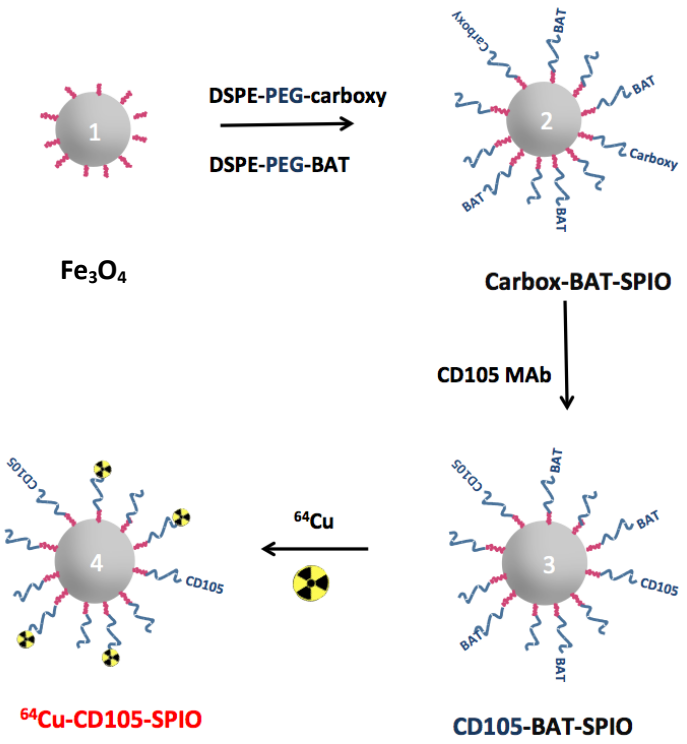

Figure 24: A schematic of the synthesis of ^{64}Cu-CD105-SPIO.

Nanoparticle Characterization

The hydrodynamic diameter of the BAT-SPIOs and BAT-CD105-SPIOs was determined via dynamic light scattering (DLS) (Malvern Instruments Zetasizer Nano ZS, UK). The SPIO solution was diluted with Millipore water (mH_2O) and size distribution data was collected at 25 ^{o}C for 30 minutes.

Surface potential of nanoparticle solutions was measured using Malvern Instruments Zetasizer Nano ZS, UK. Samples were measured in triplicate at 25 ^{o}C. Iron concentration was determined using the Ferrozine assay.

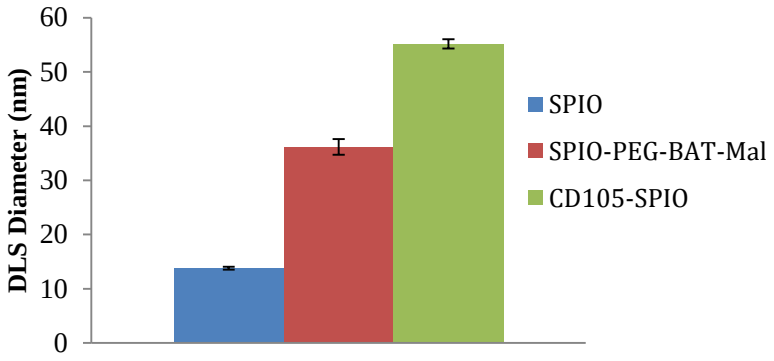

Figure 25: Size distribution of BAT-SPIOs and BAT-CD105-SPIOs using DLS

Figure 23 shows the DLS diameter after step-by-step surface modification. The addition of DSPE-PEG coating increases the size to about 38 nm and further conjugation of the antibody increased the final size to 52 nm.

In vitro studies with CD105 Targeted SPIOs

In vitro cell binding assays were employed to evaluate the CD105 targeting of CD105 conjugated SPIOs. HUVECs known to express high levels of endoglin were incubated for 1 hr at 37 ^{o}C with 50 ug/ml of DiI labeled CD105-SPIOs or Non-targeted SPIOs.

HUVECs were seeded at 2x10^{4} cells per well in T25 plates 2-3 days prior to incubation and grown in medium supplemented with 1-% fetal bovine serum (FBS) and antibiotics (penicillin/streptomycin). After incubation for 1 h at 37°C and 5% CO_2, cells were fixed for 15 min at room temperature using 4% paraformaldehyde in PBS. Nucleus was stained with Hoescht (Invitrogent). PBS was added to the cells and fluorescent

images were acquired using a Zeiss LSM microscope with a 40X water-immersion objective.

Binding of CD105-SPIOs to HUVECs was observed, while no significant binding of non-targeted SPIOs occurred (Figure 24). Binding of CD105-SPIOs to HUVECs was blocked by the addition of 5 uM of CD105 antibody to the media during incubation.

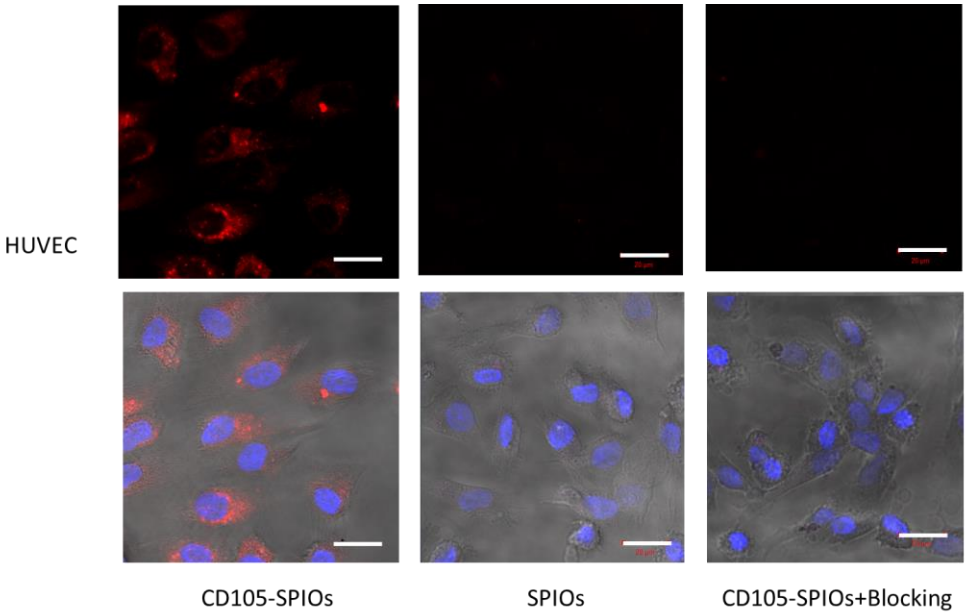

Figure 26: In vitro investigation of SPIOs in CD105 positive HUVECs using confocal microscopy. (scale bar = 20 µm)

CD105-SPIOs were also incubated with MCF7 cells and imaged following subsequent washing. Incubating CD105-SPIOs with MCF-7 cells (CD105 negative) only showed background fluorescence level. Overall these results show that DiI labeled CD105-SPIOs exhibit strong and specific binding to CD105 positive cells. This is important in moving forward with further *in vivo* investigation of CD105-SPIOs.

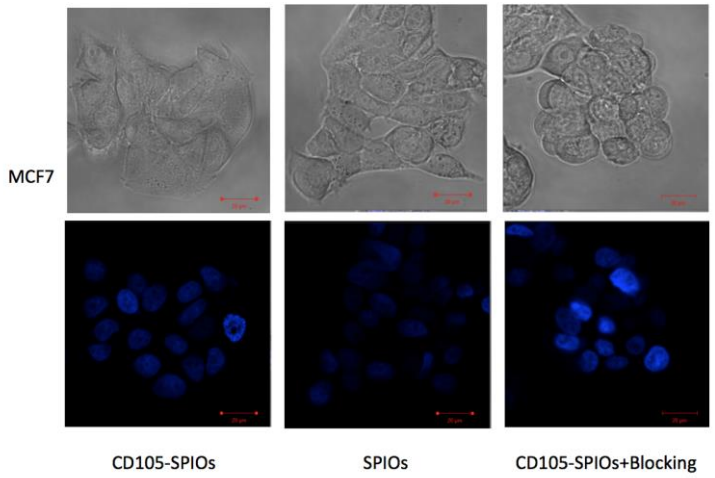

Figure 27: In vitro investigation of SPIOs in CD105 negative cells using confocal microscopy. (scale bar = 20 μm)

Phantom Studies

MRI and PET imaging capability of ^{64}Cu-CD105-SPIOs were evaluated using them same MRI and PET systems used for in vivo imaging of tumor. A nanoparticle imaging phantom was prepared and used in T2 weighted MR scan. As shown in Figure 26, a change in contrast is observed with the change in iron concentration from 10 to 100 μgFe/mL. The PET image shows the corresponding concentration dependent signal intensity. The detection threshold for ^{64}Cu-CD105-SPIOs was determined to be 10 μgFe/mL which is equivalent to 2 x 10^9 nanoparticles.

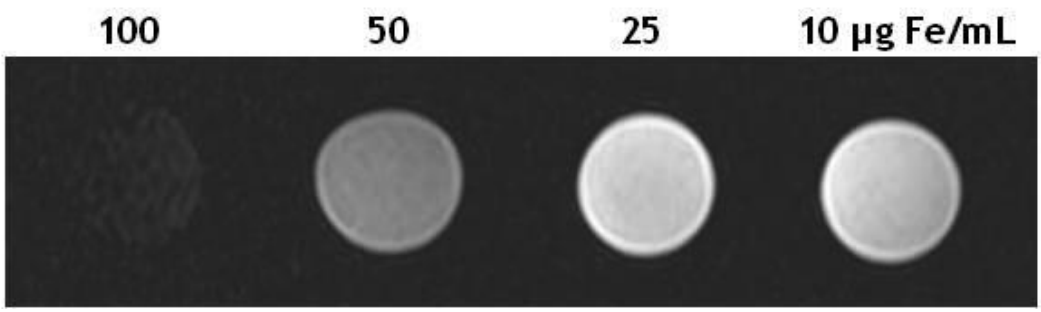

Figure 28: Characterization of CD105 SPIOs. Phantom MR image of nanoparticles.

Radiolabeling and characterization

After ^{64}Cu labeling, the SPIO sample was subjected to both radioTLC and radioFPLC analysis. The yield was about 76% before purification. Four rounds of filter centrifugation were performed to remove the free ^{64}Cu-EDTA resulting in RPC of 96% as shown in Figure 27.

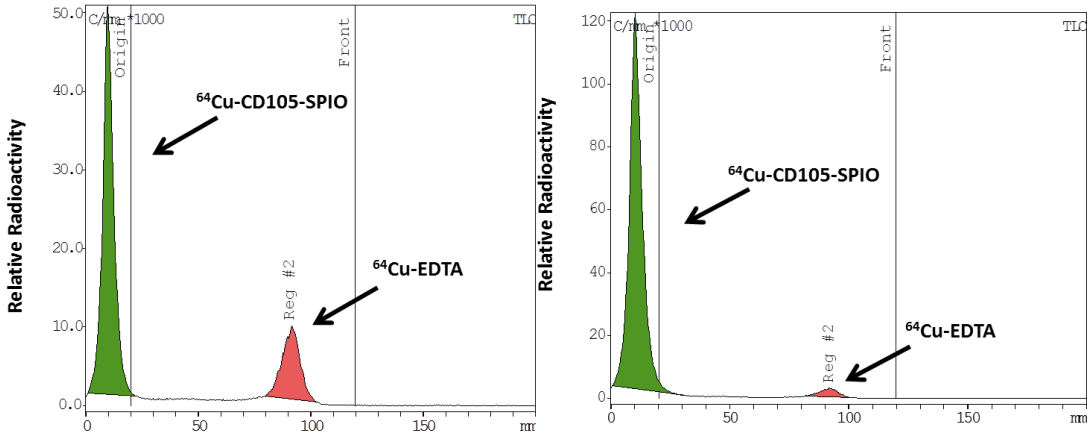

Figure 29: RadioTLC analysis of crude sample of ^{64}Cu-CD105-SPIO before and after purification.

4T1 Tumor Model

There are several reasons that the 4T1 tumor was selected as a suitable experimental animal model. First, the tumor cell line that is highly tumorigenic and invasive are easily transplanted into the mammary gland so that the primary in the correct anatomical site. Second, the progressive spread of the 4T1 metastases to the lymph nodes and other organs is very similar to that of human mammary cancer. Also, the 4T1 metastatic disease develops spontaneously from the primary tumor [42].

All animal studies were conducted under a protocol approved by Emory University Institutional Animal Care and Use Committee. Female BALB/c mice that were 4-5 weeks old were purchased from Harlan (Indianapolis, IN, USA). The 4T1 model was developed by subcutaneously injecting 2 x 104 cells suspended in 100 uL of cells suspended in PBS into the front flank of mice. The tumor size was monitored every day and the animals were subjected to in vivo experiments when the tumor diameter reached 5-8mm as shown in Figure 28.

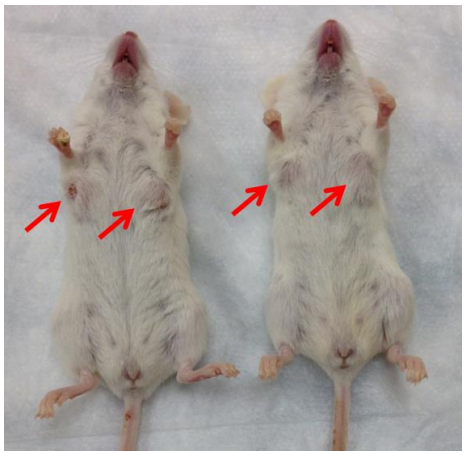

Figure 30: Female BALB/c mice with two 4T1 tumors shown with red arrows.

PET Imaging and Biodistribution studies of CD105 Targeted SPIOs

The PET/CT scans at various time points post injection were performed using a microPET/microCT scanner (Inveon rodent model, Siemens Medical Solutions USA, Inc.). Image reconstruction, and ROI analysis of the PET data were performed using AsiPro software. Tumor bearing mice were each injected a 0.1mgFe/kg dose (50 uCi) of ^{64}Cu-CD105-SPIOs (n=3) or ^{64}Cu-SPIOs (n=3) via retro orbital before serial PET scans. After the PET scan at 24 hr post injection, biodistribution studies were carried to obtain the %ID/g values in tumor and other major organs. In each group (targeted and non-targeted) 3 mice were euthanized, blood, 4T1 tumors and major organs and tissues were collected and weighed. The radioactivity in the tissue was measured using a gamma-counter (Perkin-Elmer) and presented as %ID/g (mean +- SD).

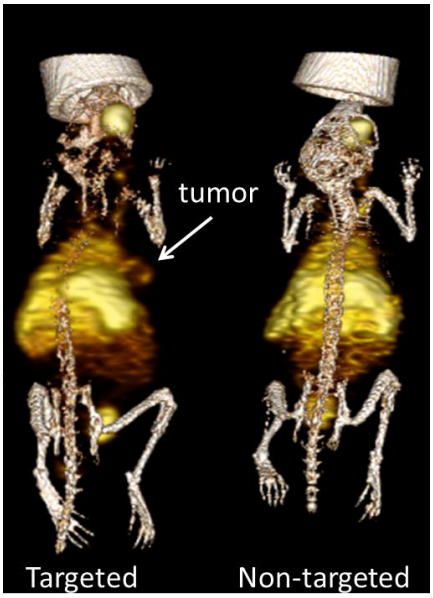

Figure 31: Representative microPET/microCT images of 4T1 tumor 1 hr post injection of ^{64}Cu-CD105-SPIOs and non-targeted ^{64}Cu-SPIOs.

As shown in Figure 29, only targeted SPIOs produced PET signal in 4T1 tumor. The non-targeted SPIOs did not produce a PET signal. Biodistribution was performed 24 hr post injection and the results were plotted as the ratio of tumor to tissue ratio (Figure 30).

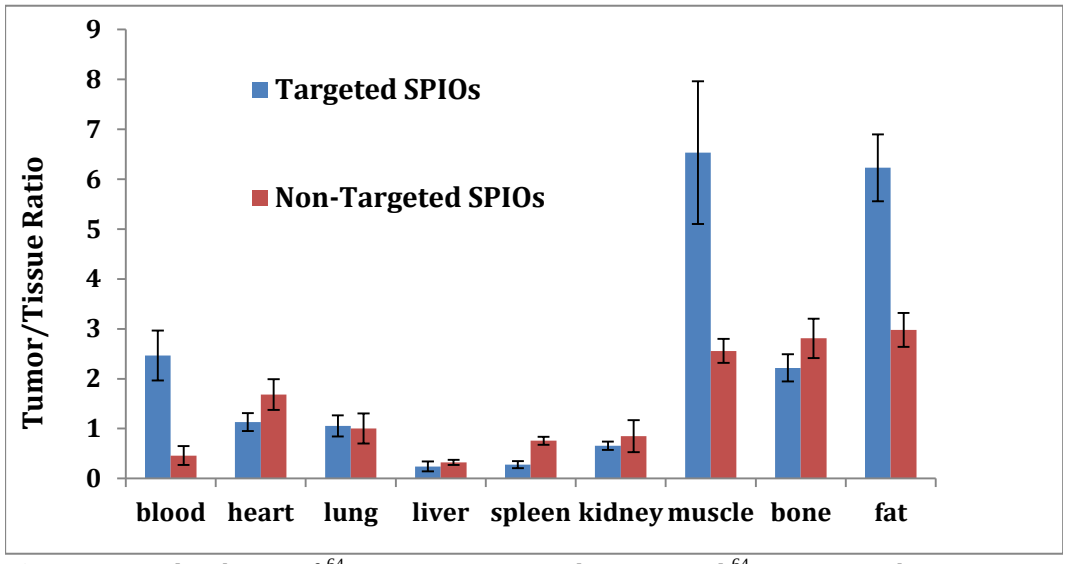

Figure 32: Biodistribution of ^{64}Cu-CD105-SPIOs and non-targeted ^{64}Cu-SPIOs 24 hr post injection in 4T1 tumor bearing mice. Results are plotted as tumor to tissue ratio.

Biodistribution of ^{64}Cu-CD105-SPIOs and ^{64}Cu-SPIOs revealed that significant RES uptake as previously observed in C57 mice. Blood activity was significantly decreased 24 hrs post injection and the tumor uptake showed a slightly higher uptake when targeted SPIOs were injected. The mice used in this study, had a very small tumors (~5mm x 1mm). ^{64}Cu-CD105-SPIOs showed significantly higher tumor to tissue ratio compared to non-targeted SPIOs. Specifically, the tissues surrounding the tumor site such as blood, muscle and fat had much higher tumor to tissue ratios as was observed in the PET/CT images.

To further allow the nanoparticles to accumulate in the tumor, two BALB/C mice were kept alive post MR imaging. These mice were injected a 0.1mgFe/kg dose of CD105-SPIOs. After one day they were re-injected a 150 uCi of ^{64}Cu-CD105-SPIOs (n=2) via retro orbital. PET imaging was performed 24 hr post injection. The results are shown in Figure 31.

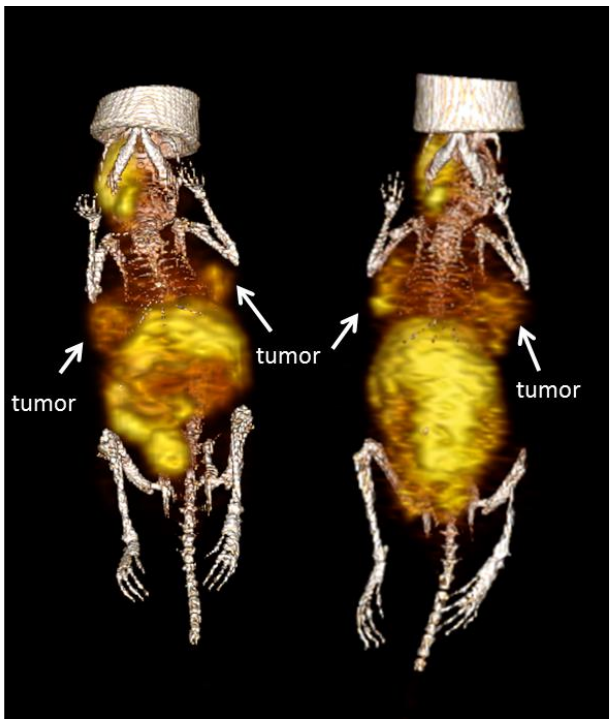

Figure 33: Representative microPET/microCT images of 4T1 tumor 24hr post injection of ^{64}Cu-CD105-SPIOs and non-targeted ^{64}Cu-SPIOs.

As it is indicated in Figure 31, the nanoparticles produced a detectable signal in both tumors. In this study the tumors were significantly larger with a diameter of about 10mm. The imaging time (24 hr post injection) produced images with much lower background especially in the liver and spleen areas. The tumor vasculature was clearly visible at this time point.

In vivo MR imaging using ^{64}Cu-CD105-SPIOs

To examine the MR imaging potential and targeting efficiency of ^{64}Cu-CD105-SPIOs, cold particles were injected to 4T1 tumor bearing mice. Animals were scanned using a multi slice multi echo sequence to obtain T_2 weighted tumor images. The images were obtained with fat suppression from 3 Tesla MR scanner (Tim/Trio, Siemens, Erlangen, Germany, TR/TE=3600/86 ms, Slice thickness=1 mm, FOV=84X120, 3 averages, total scan time=183ms). Tumor bearing mice were imaged pre-injection of nanoparticles.

A single dose of CD105-SPIOs (n=3) or non-targeted SPIOs (n=3) were then injected (0.1mgFe/kg) via tail vein injection and animals were imaged at 24 hr post injection. T_2 weighted images of tumors after injection show a negative contrast enhancement compared to pre injection images as shown in Figure 32. Analysis of the corresponding multi echo T_2 maps showed that the decrease in the mean tumor T_2 post injection of SPIOs. The decrease in the mean tumor T_2 produced by CD105 targeted SPIOs was less than the decrease produced by non-targeted SPIOs.

Figure 34: Representative MR images of 4T1 tumor 24 hr post injection of ^{64}Cu-CD105-SPIOs and non-targeted ^{64}Cu-SPIOs.

Discussion and Conclusion

To achieve sufficient in vivo stability and tumor targeting it is important to modify the surface of the SPIOs. This is achieved by the simplified reaction scheme of coating the Fe_3O_4 cores with DSPE-PEG2k-carboxy and PEG-lipid-BAT. Conjugation of CD105 antibody using EDAC was then performed before radiolabeling. The reaction was performed overnight at 4^{o}C. In this synthetic scheme surface PEGylation was perfomed once with the incorporation of PEG-caroboxy and PEG-lipid-BAT. This method significantly improved the radiolabeling yield and eliminated one post conjugation step. We then performed comprehensive characterizations of size and surface charge with DLS, TEM and zeta potential to ensure successful surface modification. The final SPIO solution was well-dispersed in PBS with no aggregation.

Serum stability studies confirmed that more than 90% of radioactivity is bound to the nanoparticle after 24 hr which ensured that the signal observed in PET studies reflects

the distribution of ^{64}Cu labeled SPIOs. We then performed quantitative biodistribution with ^{64}Cu-CD105-SPIOs and non-targeted ^{64}Cu-SPIOs. The results were plotted as tumor to tissue ratios and showed that the CD105 targeted SPIOs had significantly higher tumor to tissue ratios for muscle, fat and blood. These results were consistent with PET imaging results for the 5 days post injection 4T1 model where we could only see the small tumor with the targeted SPIOs. In this case, the tumor reached a size of about 5 mm x 1 mm after 5 days and PET imaging was performed for 60 min right after injection. Longer wait time between injection and imaging could have improved the uptake in the tumor since nanoparticles have a blood circulation half-life about 35 min. Biodistribution was performed by sacrificing the mice 24 hrs post injection, and we found that about 4.2% injected dose per gram accumulates in the tumor for ^{64}Cu-CD105-SPIOs. The non-targeted ^{64}Cu-SPIOs had about 3.2% injection dose per gram in the tumor after 24 hrs. Active targeting mediated by affinity ligands may complement EPR (enhanced permeability and retention) or provide an alternative delivery mechanism. SPIO nanoparticles with their multivanlency can help overcome the weak affinity of some ligand antigen pairs. As shown in this work, the addition of CD105 antibody can increase the tumor uptake by 50%. This increase in uptake is mainly due to the uptake by tumor neuvasculature endothelial cells overexpressing endoglin. This is the first report of PET/MR imaging with dual modality ^{64}Cu-CD105-SPIOs targeted to endoglin. As shown through *in vitro* and *in vivo* experiments ^{64}Cu-CD105-SPIOs exhibited stability and target specificity. The significant finding was the high contrast of SPIOs on the clinical 3 Tesla MR scanner. An approximately 50% increase in tumor uptake was observed when using active targeting compared to passive targeting based only on EPR effect. By taking

advantage of MR soft tissue contrast and PET sensitivity, dual modality SPIOs have a great potential in early stage detection of breast cancer tumors. To further evaluate the potential of CD105-SPIOs it may be necessary to continue the dual PET/MR imaging studies with multiple injection of cold and hot nanoparticles. IHC studies on tumor and muscle tissues are also required to quantify the amount of CD105 expression. Also, PCR studies are recommended to correlate the expression level of endoglin with the uptake of targeted SPIOs.

Endoglin maybe overexpressed on the neuvasculature endothelial cells in other diseases such as atherosclerotic plaque. This could potentially cause problems with increasing false positives.

Radiolabeled nanoparticles conjugated to anti-CD105 antibodies can further enhance diagnostic and prognostic imaging for tumors by highlighting the tumor vasculature, as well as provide a universal contrast agent. The development of ^{64}Cu-SPIOs targeting CD105 that can be used in PET/MR multimodal imaging would allow for significantly improved diagnostics. Although these studies focused on the *in vitro* cellular uptake and *in vivo* molecular imaging of anti-CD105 antibodies conjugated to SPIOs, one class of this antibody (TRC105) is currently in phase II clinical trial for treating glioblastoma, kidney, and liver cancer.

References

19. R. Siegel, J. Ma, Z. Zou, and A. Jemal, “Cancer Statistics, 2014,” vol. 64, no. 1, pp. 9–29, 2014.

20. S. E. Duff, C. Li, J. M. Garland, and S. Kumar, “CD105 is important for angiogenesis: evidence and potential applications.,” FASEB J., vol. 17, no. 9, pp. 984–92, Jun. 2003.

21. E. Fonsatti, M. Altomonte, M. R. Nicotra, P. G. Natali, and M. Maio, “Endoglin (CD105): a powerful therapeutic target on tumor-associated angiogenetic blood vessels.,” *Oncogene*, vol. 22, no. 42, pp. 6557–63, Sep. 2003.

22. J. Fang, H. Nakamura, and H. Maeda, “The EPR effect: Unique features of tumor blood vessels for drug delivery, factors involved, and limitations and augmentation of the effect.,” *Adv. Drug Deliv. Rev.*, vol. 63, no. 3, pp. 136–51, Mar. 2011.

23. C. Li, R. Issa, P. Kumar, I. N. Hampson, J. M. Lopez-Novoa, C. Bernabeu, and S. Kumar, “CD105 prevents apoptosis in hypoxic endothelial cells.,” *J. Cell Sci.*, vol. 116, no. Pt 13, pp. 2677–85, Jul. 2003.

24. K. Kinkel, “Detection of hepatic metastases from cancers of the gastrointestinal tract by using noninvasive imaging methods (US, CT, MR imaging, PET): a meta-analysis,” *Radiology*, vol. 224, no. 3, pp. 748–56, 2002.

25. J. Czernin, M. Allen-Auerbach, and H. R. Schelbert, “Improvements in cancer staging with PET/CT: literature-based evidence as of September 2006.,” *J. Nucl. Med.*, vol. 48 Suppl 1, no. September 2006, p. 78S–88S, Jan. 2007.

26. B. Chertok, B. a Moffat, A. E. David, F. Yu, C. Bergemann, B. D. Ross, and V. C. Yang, “Iron oxide nanoparticles as a drug delivery vehicle for MRI monitored magnetic targeting of brain tumors.,” *Biomaterials*, vol. 29, no. 4, pp. 487–96, Feb. 2008.

27. V. C. Y. Beata Chertok, Adam J. Cole, Allan E. David, “Comparison of electron spin resonance spectroscopy and inductively-coupled plasma optical emission spectroscopy for biodistribution analysis of iron-oxide nanoparticles,” *Mol. Pharm.*, vol. 7, no. 2, pp. 375–385, 2010.

28. R. a Brekken, C. Li, and S. Kumar, “Strategies for vascular targeting in tumors.,” *Int. J. Cancer*, vol. 100, no. 2, pp. 123–30, Jul. 2002.

29. C. Li, “A targeted approach to cancer imaging and therapy,” *Nat. Material.*, vol. 13, no. 2, pp. 110–115, Jan. 2014.

30. F. Chen, H. Hong, Y. Zhang, and H. Valdovinos, “In vivo tumor targeting and image-guided drug delivery with antibody-conjugated, radiolabeled mesoporous silica nanoparticles,” *ACS Nano*, vol. 7, no. 10, pp. 9027–9039, 2013.

31. D. Neri and R. Bicknell, “Tumour vascular targeting.,” *Nat. Rev. Cancer*, vol. 5, no. 6, pp. 436–46, Jun. 2005.

32. A. S. Chi, a G. Sorensen, R. K. Jain, and T. T. Batchelor, “Angiogenesis as a therapeutic target in malignant gliomas.,” *Oncologist*, vol. 14, no. 6, pp. 621–36, Jun. 2009.

33. D. G. Duda, T. T. Batchelor, C. G. Willett, and R. K. Jain, “VEGF-targeted cancer therapy strategies: current progress, hurdles and future prospects.,” *Trends Mol. Med.*, vol. 13, no. 6, pp. 223–30, Jun. 2007.

34. E. Fonsatti, H. J. M. Nicolay, M. Altomonte, A. Covre, and M. Maio, “Targeting cancer vasculature via endoglin/CD105: a novel antibody-based diagnostic and therapeutic strategy in solid tumours.,” *Cardiovasc. Res.*, vol. 86, no. 1, pp. 12–9, Apr. 2010.

35. E. Fonsatti and M. Maio, “Highlights on endoglin (CD105): from basic findings towards clinical applications in human cancer.,” *J. Transl. Med.*, vol. 2, no. 1, p. 18, Jun. 2004.

36. H. Hong, K. Yang, Y. Zhang, J. Engle, and L. Feng, “In vivo targeting and imaging of tumor vasculature with radiolabeled, antibody-conjugated nanographene,” *ACS Nano*, vol. 6, no. 3, pp. 2361–2370, 2012.

37. S. Shi, K. Yang, H. Hong, H. F. Valdovinos, T. R. Nayak, Y. Zhang, C. P. Theuer, T. E. Barnhart, Z. Liu, and W. Cai, “Tumor vasculature targeting and imaging in living mice with reduced graphene oxide.,” *Biomaterials*, vol. 34, no. 12, pp. 3002–9, Apr. 2013.

38. Y. Zhang, H. Hong, J. W. Engle, Y. Yang, C. P. Theuer, T. E. Barnhart, and W. Cai, “Positron emission tomography and optical imaging of tumor CD105 expression with a dual-labeled monoclonal antibody.,” *Mol. Pharm.*, vol. 9, no. 3, pp. 645–53, Mar. 2012.

39. K. Tao, M. Fang, J. Alroy, and G. G. Sahagian, “Imagable 4T1 model for the study of late stage breast cancer.,” *BMC Cancer*, vol. 8, p. 228, Jan. 2008.

40. D. Zhang, X.-Y. Feng, T. D. Henning, L. Wen, W.-Y. Lu, H. Pan, X. Wu, and L.-G. Zou, “MR imaging of tumor angiogenesis using sterically stabilized Gd-DTPA liposomes targeted to CD105.,” *Eur. J. Radiol.*, vol. 70, no. 1, pp. 180–9, Apr. 2009.

41. L. S. Rosen, H. I. Hurwitz, M. K. Wong, J. Goldman, D. S. Mendelson, W. D. Figg, S. Spencer, B. J. Adams, D. Alvarez, B. K. Seon, C. P. Theuer, B. R. Leigh, and M. S. Gordon, "A phase I first-in-human study of TRC105 (Anti-Endoglin Antibody) in patients with advanced cancer.," *Clin. Cancer Res.*, vol. 18, no. 17, pp. 4820–9, Sep. 2012.

42. L. Fass, "Imaging and cancer: a review.," *Mol. Oncol.*, vol. 2, no. 2, pp. 115–52, Aug. 2008.

43. Z. Cheng, A. Al Zaki, J. Z. Hui, V. R. Muzykantov, and A. Tsourkas, "Multifunctional nanoparticles: cost versus benefit of adding targeting and imaging capabilities.," *Science*, vol. 338, no. 6109, pp. 903–10, Nov. 2012.

44. S. Cherry, "Multimodality imaging: Beyond pet/ct and spect/ct," *Semin. Nucl. Med.*, vol. 39, no. 5, pp. 348–353, 2009.

45. Y. Xing, J. Zhao, P. Conti, and K. Chen, "Radiolabeled Nanoparticles for Multimodality Tumor Imaging," *Theranostics*, vol. 4, no. 3, pp. 290–306, 2014.

46. C. Glaus, R. Rossin, M. J. Welch, and G. Bao, "In vivo evaluation of (64)Cu-labeled magnetic nanoparticles as a dual-modality PET/MR imaging agent.," *Bioconjug. Chem.*, vol. 21, no. 4, pp. 715–22, Apr. 2010.

47. R. F. Minchin and D. J. Martin, "Nanoparticles for molecular imaging--an overview.," *Endocrinology*, vol. 151, no. 2, pp. 474–81, Feb. 2010.

48. S. Tong, S. Hou, Z. Zheng, J. Zhou, and G. Bao, "Coating optimization of superparamagnetic iron oxide nanoparticles for high T2 relaxivity.," *Nano Lett.*, vol. 10, no. 11, pp. 4607–13, Nov. 2010.

49. C. Zhang, M. Jugold, E. C. Woenne, T. Lammers, B. Morgenstern, M. M. Mueller, H. Zentgraf, M. Bock, M. Eisenhut, W. Semmler, and F. Kiessling, "Specific targeting of tumor angiogenesis by RGD-conjugated ultrasmall superparamagnetic iron oxide particles using a clinical 1.5-T magnetic resonance scanner.," *Cancer Res.*, vol. 67, no. 4, pp. 1555–62, Feb. 2007.

CHAPTER 5

CONCLUSIONS AND FUTURE DIRECTIONS

The combination of PET, CT and MRI offers opportunities beyond the use of single imaging modality. The synergistic effects of high sensitivity imaging of PET with high resolution soft tissue imaging of MRI can lead to easier and improved diagnosis. The dual modality contrast agent provides a platform for PET/MR contrast agents which can also be targeted. We report the development, in vitro and in vivo imaging of plaque and tumor using a novel targeted PET/MR nanoparticle. The core of the nanoparticles is made of Fe_3O_4 which is superparamagnetic due to its size being less than 20 nm. High resolution MRI imaging can be performed with high sensitivity when using these SPIOs. In addition, radioisotope ^{64}Cu was labeled on the surface of the PEG coating to perform PET imaging. Although, ^{64}Cu has a half-life of about 12.7 hrs, there are other radioisoptopes with shorter half-lives that could have been used. Fluorine-18 is one such isotope with a half-life of 109 minutes, it has the ideal properties for labeling SPIOs. The high percentage (39%) of beta decays by ^{64}Cu raises a concern regarding potential toxicity. Therefore, ^{18}F is a great alternative since it decays by positron emission 97% of the time.

There are several chelators with high affinity for ^{64}Cu such as DOTA, NOTA, and TETA. Initially, we observed that DOTA conjugation via the NHS, amine reaction causes the aggregation of the nanoparticles before the reaction is complete. This was mainly due to the low pH of the DOTA-NHS solution dissolved in water. We learned that dissolving the SPIOs at a concentration of 1 mg/ml (1 ml) in phosphate buffer at pH 7.4 before drop wise addition of the DOTA-NHS is the key in preventing the aggregation. However, the

low radio labeling yield of only 50% was an area we could improve upon. The alternative was to pre-conjugate and purify PEG to the chelator and use it during coating. Lipid-PEG-BAT was already synthesized and used in imaging liposomes and was sent to us from Dr. Ferrara's laboratory at UC Davis. BAT is a derivative of TETA which has higher affinity for ^{64}Cu compared to DOTA. Using only 2% lipid-PEG-BAT, we reached 95% radiolabeling yield and a method for the addition of targeting ligand. This simplified method was used in developing both tumor targeting and VCAM1 targeting of inflammation.

^{64}Cu-VINP-SPIOs showed great potential in imaging VCAM1 overexpression in the carotid ligation model of inflammation. Although additional studies maybe required to confirm the specificity of targeting, the *in vivo* results with scramble version of the peptide served as a decent control. In this case, the ratio of LCA to RCA SUV uptake showed was higher when using targeted SPIOs compared to scramble and non-targeted SPIOs. Blocking studies with the pre injection of VCAM antibody alone can be beneficial in providing further evidence that the targeting is specific. To further evaluate the targeting specificity of the VINP-SPIOs, it is important to perform immunohistochemistry studies to confirm the expression of VCAM1 in the ligation area. Fluorescence microscopy may also be used with the DiI labeled SPIOs to study the colocalization of the SPIOs with different types of cells. In our initial studies we found that SPIOs get internalized into endothelial cells as well as smooth muscle cells. The information from PET/CT imaging can help determine the AHA lesion stage. If there is VCAM1 overexpression, VINP-SPIOs will indicate their presence corresponding to AHA

lesion 1. Although this information can be useful in identifying the lesion, it can fully evaluate the severity of disease.

Although we have an estimate on the number of CD105 antibodies per particle based on the initial amount of PEG-maleimide, it is recommended that the supernatant be tested before and after conjugation of the antibody to precisely quantify this number.
In the three aims of this thesis, the field of PET MR molecular imaging has been advanced by the development of protocols for the synthesis and coating of dual modality SPIO nanoparticles which are both radiolabeled and targeted to a specific antigen. This simplified synthetic scheme allows for development of imaging agents for early stage detection of inflammation. In addition, this nanoparticle can be used for multi modal, PET/MR imaging of tumor microvasculature. We have shown that targeted ^{64}Cu SPIOs are a versatile system that combines the advantages of MR and PET contrast agents. Because of their potential we studied their *in vivo* biodistribtion following interavenous injection. Experimental results revealed that SPIOs have an ability to provide contrast on a clinical 3 Tesla MR scanner in addition to producing high signal intensity in pre-clinical PET system. These features make the SPIOs an ideal candidate to be transferred to clinic for clinical diagnosis of diseases such as inflammation and cancer.

To publicize these advancements we are planning to publish our work in the following research articles:

Masoodzadehgan N, Seo W, Virani N, Gray S, Weiss D, Seo J, Goodman M, Taylor B, Ferrara K, Bao G. 2014. "Multi modal plaque imaging with VCAM targeted ^{64}Cu-SPIOs" *Manuscript in preparation.*

Masoodzadehgan N, Gray S, Bao G. 2014. "Nanoparticle Size Review"
In the submission process.

Masoodzadehgan N, Seo W, Virani N, Gray S, Weiss D, Seo J, Goodman M, Taylor B, Ferrara K, Bao G. 2014. "PET-MR imaging of tumor CD105 expression using targeted ^{64}Cu –SPIOs"
Manuscript in preparation.

Several conference posters and presentations created collaborations with colleagues in cardiology, imaging, and radiochemistry. To further explore plaque imaging, we are currently synthesizing ^{64}Cu-VINP-SPIOs to perform biodistirbution and PET/MR imaging studies in a rabbit ligation model. The amount of nanoparticles produced needs to be scaled up to perform these studies. Each rabbit weights about 2 kg and that is 100 times the weight of the mice used in our previous imaging studies.

We have also developed a collaboration with Dr. Hui Mao's laboratory at Emory University. We are planning to continue this collaboration to further understand the effect of targeting on PET/MR imaging of 4T1 tumor. Taking advantage of the 3 Tesla MR system at Wesley Woods, we can analyze the effect of targeting on imaging breast cancer tumors. This scanner is currently used for clinical scans and it can provide valuable information when used in pre-clinical validation studies.

APPENDIX A:

Synthesis of BAT-PEG-lipid. The ^{64}Cu-specific chelator, 6-[*p*-(bromoacetamido)benzyl]-1,4,8,11-tetraazacyclotetradecane-*N*,*N*′,*N*″,*N*‴-tetraacetic acid (BAT), was conjugated with an artificial lipid to form a BAT-PEG-lipid coating using Fmoc solid phase synthesis. The synthesis was conducted following methods from Katherine W. Ferrara's laboratory at the University of California, Davis. Initially, Fmoc-Cys(Mnt)-OH, Fmoc-NH-(PEG)27-COOH, Fmoc-Lys(Fmoc)-OH, and stearic acid were serially added to PAL-PEG-PS resin. Next, the protective Mnt group was removed with 1% TFA/DCM. The unprotected resin was then coupled with the BAT in a DMF/DMSO/H_2O (1:1:1 v/v/v) solvent, pH of 8. The pH was adjusted with DIPEA, and the reaction was monitored with DTNP solution. The resulting product was cleaved by a TFA/TIPS/H_2O solvent (9.5:2.5:2.5 v/v/v). After cleaving, the product was purified via reversed-phase high performance liquid chromatography (HPLC) and the mass was confirmed via matrix-assisted laser desorption/ionization (MALDI).

Iron measurement via Ferrozine Assay. The iron content of the SPIOs was determined by mixing 50 µL of dilute SPIO solution with 50 µL of 12M HCl for 30 minutes at room temperature on a shaker. Next, the solution was mixed with 240 µL of 2M NaOH, 50 µL of 4N ammonium acetate, and 110 µL of 5% hydroxylamine HCl for 30 minutes. After incubation, 50 µL of sample was mixed with 50 µL of 0.1% ferrozine solution and incubated for 15 minutes. Absorbance was read at 562 nm with 810 nm as reference.

Characterization via Transmission Electron Microscopy (TEM). ^{64}Cu-VINP-SPIO were analyzed after three weeks post radiolabeling. A 5 µl sample suspension of both 6nm and 14nm SPIOs were place on a 400 mesh carbon coated copper grid that had been made hydrophilic by glow discharge. After 5 minutes, grid with the sample was dragged by the side of grid on a piece of filter paper. For negative staining, 5 µl of 1% aqueous methylamine tungstate (MAT) or phosphotungstic acid (PTA) was applied onto grid immediately after sample removal, and then removed as described above after 30 seconds. Grid was let completely dry before microscopy view using a Hitachi H 7500 TEM.

APPENDIX B:

Chapter 4:

Biodistribution tables

Table1: Organ biodistribution of 6nm ^{64}Cu-SPIOs (control) as % injected dose per gram tissue.

15 min pi	blood	heart	lung	liver	spleen	kidney	muscle	brain	bone	fat
avg	44.22%	5.07%	6.54%	5.51%	11.47%	8.65%	0.74%	0.73%	1.65%	0.72%
std dev	7.65%	1.09%	1.34%	1.08%	2.88%	1.67%	0.13%	0.16%	0.45%	0.13%
1 hr pi										
avg	26.25%	3.10%	4.76%	19.62%	13.35%	6.53%	0.52%	0.55%	2.25%	0.66%
std dev	2.94%	0.60%	0.55%	3.14%	0.43%	0.85%	0.07%	0.09%	0.42%	0.34%
3 hr pi										
avg	21.81%	2.62%	3.30%	25.16%	16.34%	5.55%	0.50%	0.48%	1.58%	0.58%
std dev	1.53%	0.28%	1.04%	3.38%	4.27%	1.02%	0.07%	0.04%	0.80%	0.05%
24 hr pi										
avg	6.33%	1.66%	2.56%	10.04%	9.96%	3.63%	0.36%	0.21%	1.18%	0.44%
std dev	3.26%	0.46%	0.60%	2.73%	1.68%	1.12%	0.09%	0.08%	0.33%	0.17%

Table2: Organ biodistribution of 6nm ^{64}Cu-VINP-SPIOs (targeted) as % injected dose per gram tissue.

15 min pi	blood	heart	lung	liver	spleen	kidney	muscle	brain	bone	fat
avg	26.57%	3.21%	5.93%	8.81%	3.96%	26.35%	0.91%	0.47%	1.41%	1.04%
std dev	0.80%	0.53%	0.85%	1.28%	0.32%	2.09%	0.13%	0.07%	0.15%	0.25%
1 hr pi										
avg	10.26%	1.83%	4.14%	18.65%	15.62%	21.14%	0.56%	0.31%	1.57%	0.80%
std dev	0.04%	0.40%	1.06%	4.47%	4.95%	2.88%	0.07%	0.07%	0.32%	0.19%
3 hr pi										
avg	4.88%	1.64%	4.47%	17.61%	9.35%	10.12%	0.69%	0.22%	1.39%	0.66%
std dev	0.32%	0.24%	0.59%	2.25%	2.24%	1.64%	0.21%	0.04%	0.37%	0.19%
24 hr pi										
avg	2.20%	1.64%	3.95%	11.25%	4.25%	6.20%	0.44%	0.26%	0.88%	0.60%
std dev	0.27%	0.20%	0.53%	1.19%	0.30%	1.11%	0.09%	0.04%	0.23%	0.14%

Table3: Organ biodistribution of 14nm ^{64}Cu-SPIOs (control) as % injected dose per gram tissue.

15 min pi	blood	heart	lung	liver	spleen	kidney	muscle	brain	bone	fat
avg	38.38%	5.96%	9.01%	9.29%	7.23%	6.78%	0.67%	1.02%	1.87%	0.99%
std dev	3.44%	1.55%	0.62%	1.62%	1.64%	0.68%	0.02%	0.24%	0.35%	0.23%
1 hr pi										
avg	22.89%	3.09%	6.11%	18.30%	23.76%	5.88%	0.55%	0.58%	1.78%	0.77%
std dev	4.63%	0.50%	1.64%	2.61%	2.77%	0.67%	0.09%	0.12%	0.46%	0.12%
3 hr pi										
avg	16.75%	2.97%	5.81%	35.32%	38.12%	5.65%	0.49%	0.40%	2.30%	0.86%
std dev	3.68%	0.43%	1.28%	6.79%	8.49%	1.14%	0.06%	0.06%	0.56%	0.16%
24 hr pi										
avg	1.01%	1.00%	2.17%	9.25%	14.14%	2.29%	0.21%	0.10%	0.99%	0.32%
std dev	0.18%	0.06%	0.19%	0.26%	3.22%	0.10%	0.03%	0.01%	0.10%	0.06%

Table4: Organ biodistribution of 14nm ^{64}Cu-VINP-SPIOs (targeted) as % injected dose per gram tissue.

15 min pi	blood	heart	lung	liver	spleen	kidney	muscle	brain	bone	fat
avg	16.04%	3.94%	9.27%	20.78%	10.46%	15.08%	0.88%	0.49%	1.86%	0.85%
std dev	2.08%	0.80%	0.75%	1.91%	0.81%	2.09%	0.14%	0.03%	0.21%	0.11%
1 hr pi										
avg	7.95%	2.74%	7.90%	23.13%	15.87%	8.78%	0.63%	0.37%	1.58%	0.75%
std dev	0.48%	0.24%	0.56%	2.48%	1.02%	0.80%	0.03%	0.03%	0.12%	0.14%
3 hr pi										
avg	5.01%	2.92%	8.93%	26.65%	15.00%	8.99%	0.60%	0.36%	1.79%	0.85%
std dev	0.57%	0.33%	0.48%	0.66%	1.23%	0.95%	0.04%	0.04%	0.19%	0.12%
24 hr pi										
avg	1.20%	2.96%	6.41%	15.16%	7.30%	7.37%	0.59%	0.45%	1.45%	0.64%
std dev	0.13%	0.25%	0.84%	1.16%	0.82%	0.78%	0.06%	0.06%	0.09%	0.13%

Chapter 5: *Ex vivo* autoradiography of carotid after injection of 50 µCi dose of ^{64}Cu-VINP-SPIOs in the carotid ligation ApoE$^{-/-}$ KO mice.

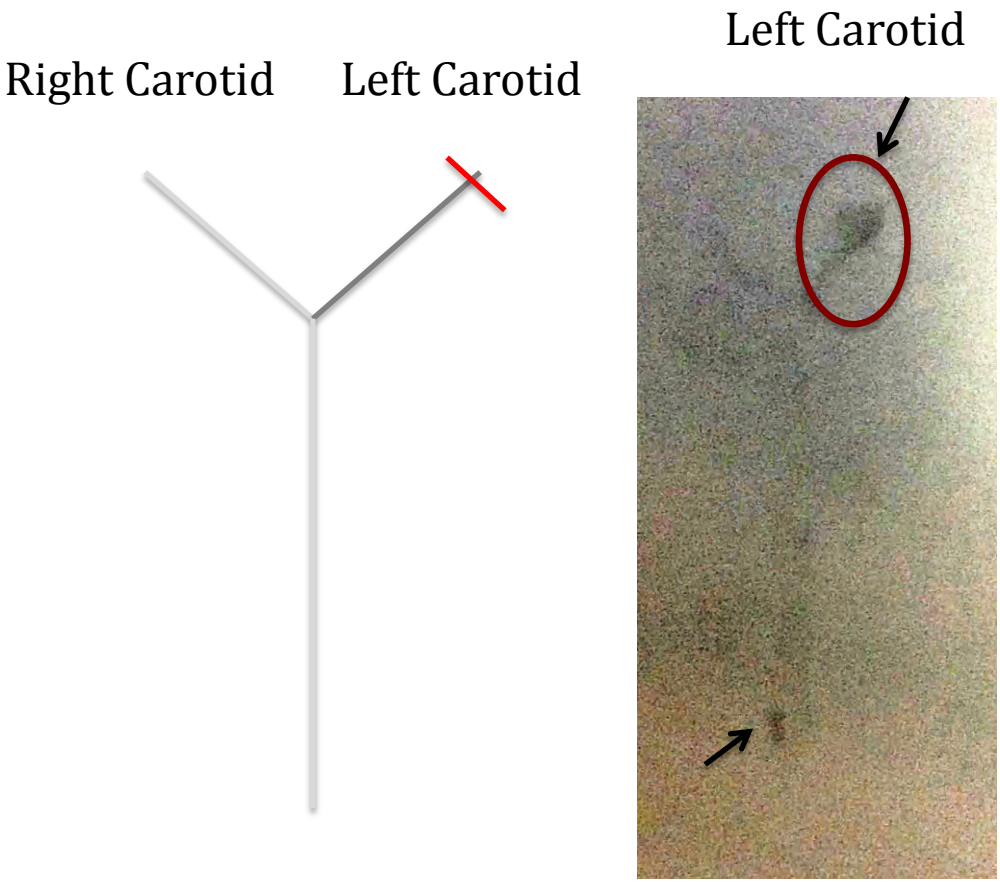

CURRICULUM VITA

Nazanin Hoshyar Masoodzadehgan

Laboratory of Biomolecular Engineering and Nanomedicine
nazanin.masood@gmail.com

EDUCATION

Georgia Institute of Technology 2008-2014
PhD Candidate in Nuclear Engineering and Medical Physics
Completed Part I of ABR certification exam
Minor in Management
PhD advisor: Dr. Gang Bao, PhD, GPA: 3.65/4.00

Georgia Institute of Technology 2008-2012
Master of Science in Medical Physics, GPA 3.60/4.00
Graduated with Highest Honor

Georgia Institute of Technology 2006-2008
Bachelor of Science in Biomedical Engineering, GPA 3.82/4.00
Graduated with Highest Honor

RESEARCH EXPERIENCE

Georgia Institute of Technology, Laboratory of Biomolecular Engineering and Nanomedicine 2008-present

- Synthesis, characterization and optimization of a targeted Superparamagnetic Iron Oxide nano particle (SPIO) for PET/MR
- Imaging atherosclerotic plaque using targeted ^{64}Cu-SPIOs
- Determination of circulation half life and biodistribution of ^{64}Cu labeled SPIOs
- Magnetic Resonance Tracking of Human Mesenchymal Stem Cells with Super Paramagnetic Iron Oxide Nano Particles
- Supervised, trained and managed undergraduate students on individual research projects 2013-present
- Presented research findings at national and international conferences

Emory University, (Dr. Hui Mao radiology lab)

- Breast cancer tumor detection using nano particle targeted multi modal imaging
- Investigate targeting specificity of antibody conjugated SPIOs Using breast cancer tumor model
- Established Materials Transfer Agreement with Tracon Pharmaceutical to develop antibody targeted
  nanoparticles for PET/MR Imaging of tumor

Emory University/Georgia Institute of Technology, (Dr. Robert Taylor cardiovascular lab) 2011-present

- Atherosclerotic plaque detection using nano particle targeted multi modal imaging
- Investigate targeting specificity of antibody conjugated SPIOs Using carotid ligation model of inflammation
- MR imaging of the Apo/E mice to detect atherosclerotic plaque

Georgia Institute of Technology/Emory University, (Dr. Mark Goodman radiopharmacy lab) 2010-present

- Development of radiolabeled dual modality PET/MR contrast agent
- Biodistribution and circulation halflife studies to understand the pharmacokinetics of the contrast agent in vivo
- microPET/microCT imaging of the mice with radio labeled SPIOs

Emory University/ Saint Joseph's Hospital of Atlanta (Medical Physics & Radiation Oncology) 2009-2009

- Observed Monthly QA of the linear accelelator
- Observed prostate brachytherapy, mammosite, prostate IMRT, eye plaque surgery
- Treatment planning for prostate IMRT, prostate brachytherapy, and breast mammosite

Undergraduate research experience (Cardiovascular fluid mechanics laboratory) 2007-2008

- Investigating the properties of aortic valve in order to develop a novel bioprosthetic heart valve
- Validation of the program modeling the mechanical forces on the bioprostehtic heart valve
- Collaborated with Neonatalogists and biomedical engineers at Northside hospital
- Developed a fully functional prototype for monitoring bubble CPAP sound in infants
- Tested the prototype on baby infant simulator and filed a 510K

SELECTED SKILLs

- Medical Physics: Monthly and annual QA, TG-51, IMRT, Brachytherapy Career Fair industry sponsorship liaison, Georgia Tech
- Materials: TEM, XPS
- Imaging: Imaging: PET, CT, MRI, FMT, NIRF
- Biology: Cellular Assays (Proliferation, Migration, Toxicity), Cryosectioning, Immunohistology, ELISA, RT-PCR, Protein Conjugation, Protein Extraction/Purification, Imaging (live cell imaging, confocal microscopy)
- Chemistry: Nanoparticle synthesis, coating
- Communication: Oral and Poster presentation, Technical Reports

LEADERSHIP EXPERIENCES

- BBUGS Industry Committee Chair 2013-present
- Career Fair industry sponsorship liaison, Georgia Tech 2013-present
- Board of NRE/MP Student Advisory, Georgia Tech 2012-present
- Committee chair of the Iranian Student Association, Georgia Tech 2012-present
- Graduate mentor for women professional mentoring program, Georgia Tech 2010-present
- Leading multiple research projects in the areas of stem cell, and in vivo imaging of atherosclerosis and cancer 2009-present
- Graduate Leadership Program, Georgia Tech 2010-present
- Graduate Women's Professional Mentor, Georgia Tech 2006-2008
- Undergraduate students mentor, Georgia Tech 2006-2008
- Student services tutor, Georgia Tech

Publications

- N. Masoodzadehgan et al. "Size effect of ^{64}Cu-SPIO nanoparticles on pharmacokinetics and biodistribution", in preparation for submission to ACS Nano
- N. Masoodzadehgan et al. **"**PET-MR imaging of tumor CD105 expression using targeted ^{64}Cu - SPIOs in preparation to for submission to ACS Nano
- N. Masoodzadehgan et al. **"**Multi modal plaque imaging with VCAM targeted $_{64}$Cu-SPIOs", in preparation to for submission to Circulation
- N. Masoodzadehgan et al. "Nanoparticle Size Review", in preparation for submission to Annual Review of Biomedical Engineering

SELECTED CONFERENCE PRESENTATIONS

- N. Masoodzadehgan et al. "In vivo imaging of inflammation using multimodal nanoparticles", *BMES,* Seattle. (**Oral Presentation**) 2013
- N. Masoodzadehgan et al. "Nanomedicine: Going Small for Big Results", Blended Research at the Library, Atlanta 2012
  (Invited Talk)

SELECTED CONFERENCE PAPERS

- N. Masoodzadehgan et al. " Atlanta Consortium Foscused on Mobile Health", PHIN, Atlanta. 2014
- N. Masoodzadehgan et al. "In vivo Imaging of Inflammation in Carotid Ligation Mouse Model Using VCAM-Targeted Nanoparticles", BMES, Seattle. 2013
- N. Masoodzadehgan et al. "PET/MR Plaque imaging using superparamagnetic nanoparticles", *WMIC,* Savannah. 2013
- N. Masoodzadehgan et al. "Dual Modality PET/MR Plaque Imaging Using Superparamagnetic Nanoparticles", *GTRIC,* Atlanta. 2013
- N. Masoodzadehgan et al. "Synthesis, functionalization and evaluation of nanoparticle probes for in vivo MR and PET imaging", *BMES,* Atlanta. 2012
- N. Masoodzadehgan et al. "Modulating Magnetic Resonance Tracking of human Mesenchymal Stem Cells with Super paramagnetic Iron Oxide Nano particles", *Regenerative Medicine Workshop*, Hilton Head. 2012
- N. Masoodzadehgan et al. "Magnetic Resonance Tracking of human Mesenchymal Stem Cells with Super paramagnetic Iron Oxide Nano particles", GTRIC, Atlanta. 2012

AWARDS and HONORS

- World Molecular Imaging Best Poster Award, Savannah 2013
- Georgia Tech Research and Innovation Conference Fellowship Award 2013
- Graduate Technical Symposium Poster Award, Georgia Tech 2013
- Graduate Leadership Program, Georgia Tech 2012
- Georgia Tech Dean's List 2006-2008
- American Cancer Society Childhood Cancer Survivor Champion scholarship 2005-2007
- Phi Theta Kappa International Honor Society 2004-2012
- Ranked top 1% in the Iran National Entrance Exam 2000

REVIEWING BOARDS

- Journal of Applied Polymer Science (Wiley)
- Medical Image Analysis (Elsevier)

PROFESSIONAL SOCIETIES

- Biomedical Engineering Society (BMES)
- The American Association of Physicists in Medicine (AAPM)
- Phi Theta Kappa (International Honor Society)

COURSE WORK

- Radiation Therapy Physics, Nuclear Physics, Radiation Dosimetry, Radiation Protection, Nuclear Medicine
- Differential Equations, Statics
- Mechanics of Material
- Fundamental principles of fluid, heat, and mass transfer

TEACHING EXPERIENCE

- Instructor of Organic Chemistry (Darton College)
- Tutor of Chemistry, Differential Equations, Statics (Georgia Tech)
- Teaching Assistant of Mechanics of Material (Georgia Tech)
- Teaching Assistant of Analytical Methods in Biomedical Engineering (Georgia Tech)
- Instructor Animal Handling Short Course (Georgia Tech)